Robust Computed Tomography with Incomplete Data

S113255 - Jacob Frøsig
S113200 - Nicolai Andre Brogaard Riis

Supervisors: Per Christian Hansen and Bill Lionheart

Kongens Lyngby
B.Sc
2. February 2014

b

Summary

This thesis provides the theoretical background for analysing the ill-posedness of X-ray tomography problems and uses this to analyse the special case of laminar tomography problems.

The first part of the thesis is devoted to describing the ill-posed characteristics of X-ray tomography problems. For this purpose we show that the deconvolution problem is ill-posed. In particular we show that small high frequent perturbations in the values of the convolution can give arbitrarily large changes in solutions to the deconvolution problem. We then relate the standard mathematical model of X-ray tomography, the Radon transform, to the deconvolution problem and show that the ill-posed properties are likely to carry over. Moreover, we show that the discretised mathematical model of X-ray tomography also exhibit the same ill-posed properties.

In the second part of the thesis, we develop a method of analysing the solvability of an X-ray tomography problem by considering how ill-posed it is. In particular we use the method to describe the ill-posed characteristics of several "toy" problems. Finally the work culminates by considering two cases of laminar tomography. Here it is shown, that the characteristics from some of the toy problems carry over to the laminar tomography problems.

Resumé

Dette eksamensprojekt beskriver den teoretiske baggrund tilhørende den analyse, der beskriver hvor *ill-posed* X-ray tomografi problemer er og benytter denne til at undersøge laminar tomografi problemer.

Den første del af projektet er dedikeret til, at beskrive de ill-posed karaktertræk af X-ray tomografi problemer. For at gøre dette viser vi, at den inverse operation af en foldning er ill-posed. Mere specifikt viser vi, at små forskydninger i foldningens værdier kan give arbitrært store ændringer til løsningen af den inverse operation. Vi relaterer da Radon transformationen til foldingen og viser at de ill-posed karaktertræk sansynligvis kan overføres. Ud over dette viser vi at den diskretiserede version of X-ray tomografi problemet også udviser de samme ill-posed karaktertræk.

I den anden del af projektet udvikler vi en analyse metode til at undersøge hvor nemt det er at løse et et X-ray tomografi problem, ved at undersøge hvor ill-posed det er. Mere specifikt bruger vi metoden til at beskrive de ill-posed karaktertræk af nogle "legetøjsproblemer". Rapporten kulminerer da med en undersøgelse af two cases af laminar tomografi problemer hvor vi viser, at karaktertrækkene i legetøjsproblemerne kan overføres til disse problemer.

Preface

This thesis was prepared at The Technical University of Denmark (DTU) and marks the completion of the bachelor degree in *Mathematics and Technology*. The thesis was jointly written by students Nicolai André Brogaard Riis and Jacob Frøsig and represents a workload of 15 ECTS points for each student. The study has been conducted under the supervision of Professor Per Christian Hansen and was carried out from September 2nd 2014 to February 2nd 2015. A significant body of the work was done during an exchange stay at The University of Manchester and was co-supervised by Professor Bill Lionheart.

The exchange was funded in part by the *Erasmus+* Scholarship 2014 and *Frk. Månssons* Scholarship 2014.

We would like to express our gratitude towards Professor Per Christian Hansen and Professor Bill Lionheart without whom this project would not have been possible. We are grateful for the warm welcome we received during our stay at the University of Manchester by the Inverse Problems Group located there. Feedback and discussions from both Professors and the group helped push our project in the right direction.

We would also like to thank Finn Frøsig, Jesper Nissen, Margit Leth Petersen and Josephine Perch Nielsen for their help with the proofreading of the thesis.

Lyngby, 2. February 2014

S113255 - Jacob Frøsig
S113200 - Nicolai Andre Brogaard Riis

Supervisors: Per Christian Hansen and Bill Lionheart

List of Symbols

The following is a list of symbols used in the thesis. It is not a complete list of all symbols used in the thesis, but rather a list of the most commonly used ones. However, if a symbol is not on the list it will be clearly defined before being used in the thesis.

Symbol	Description	Space
A	The transformation matrix	$A \in \mathbb{R}^{m \times n}$
$\mathbf{a_i}$	A row vector designating the ith row in the transformation matrix, A.	$\mathbb{R}^{1 \times n}$
a_{ij}	The jth element of $\mathbf{a_i}$	$\mathbb{R}$
$\mathbf{b}$	The discrete measurements / sinogram	$\mathbb{R}^{m \times 1}$
$\mathbf{b}_\varepsilon$	The measurements with perturbations	$\mathbb{R}^{m \times 1}$
b_i	The ith element of $\mathbf{b}$	$\mathbb{R}$
C_A	The condition number of the matrix, A.	$\mathbb{R}$
d	The detector size	$\mathbb{R}$
f	The model parameter describing some property of the object	L^2
$\mathcal{F}$	The Fourier transform operator	$L^1 \to L^1$
$\hat{f}$	The Fourier transformation of $f \in L^1$	L^1
f^0	The true continuous model parameters	L^2
f_ϵ	The solution to the inverse problem with perturbed measurements	L^2
g	The continuous measurements.	L^2
g_ϵ	The continuous measurements with perturbations	L^2
$\hat{\imath}$	The imaginary unit, $\hat{\imath} = \sqrt{-1}$	

Symbol	Description	Space
I_0	The initial intensity of an X-ray beam	$\mathbb{R}$
I	The damped intensity of an X-ray beam	$\mathbb{R}$
K	The kernel of the first-kind Fredholm integral equation	L^2
$\mathcal{K}$	The integral transformation defined by the first-kind Fredholm integral equation	$L^2 \to L^2$
$\widehat{K}$	The Fourier transformation of K	L^1
$\mathbb{L}$	The collection of points on a line	$\mathbb{R}^2$
m	The number of projections	$\mathbb{R}$
n	The number of elements in the object, $\mathbf{x}$	$\mathbb{R}$
p	The projection of a beam	$\mathbb{R}$
$\mathcal{R}$	The Radon transformation	
r	The rank of the transformation matrix, A.	$\mathbb{R}$
s	The distance from the origin to a line $\mathbb{L}(s, \theta)$	$\mathbb{R}$
u_i	Left singular function from the SVE	L^2
$\mathbf{u}_i$	The ith left singular vector of the SVD	$\mathbb{R}^{m\times 1}$
U	Matrix containing left singular vectors	$\mathbb{R}^{m\times m}$
v_i	Right singular functions from the SVE	L^2
$\mathbf{v}_i$	The ith right singular vector of the SVD	$\mathbb{R}^{n\times 1}$
V	Matrix containing right singular vectors	$\mathbb{R}^{n\times n}$
$\mathbf{x}$	The object/image	$\mathbb{R}^{n\times 1}$
$\mathbf{x}^{\text{exact}}$	The exact object	$\mathbb{R}^{n\times 1}$
x_i	The ith element of the object	$\mathbb{R}$
$\mathbf{x}_\varepsilon$	The object from the system with perturbation in the measurements	$\mathbb{R}^{n\times 1}$
α	Scaling parameter used for rectangular and laminar domains	$\mathbb{R}$
γ	The variable in frequency domain	$\mathbb{R}$
δ	The Dirac delta function	
ϵ	Pertubation in continuous measurements	L^2
ε	The discrete perturbation	$\mathbb{R}^{m\times 1}$
η	The relative noise level	$\mathbb{R}$
θ	An angle	$[0, \pi[$
κ	Translation parameter used for laminar object	$\mathbb{R}$
μ_i	Singular value from the SVE	$\mathbb{R}$
σ_i	The singular values of the SVD	$\mathbb{R}$
$\sigma_i^{(n)}$	The singular values using from the SVD using n pixels in the discretisation.	$\mathbb{R}$
ϕ, ψ	Arbitrary functions used to describe notation.	L^2
$\langle \cdot, \cdot \rangle$	The inner product	
$\| \cdot \|$	The norm	
$K * f$	The convolution of K and f	

Contents

Chapter 1

Introduction

Tomoraphy, the method of describing an image from a set of projections, was independently developed among several researchers in the early 20th century [1]. Computed tomography (CT) is a mathematical method of tomography, where an object or image is reconstructed from measurements of its projections. The application of CT is used in many fields today, such as medical imaging, due to its non destructive examination properties. In this thesis we will focus on the specific case of X-ray CT, or X-ray tomography, where the goal is to recover the interior of a body using external measurements of X-rays having passed through the body.

The goal of this thesis is to study the solvability of both general and specific X-ray tomography problems. The goal is carried out, in part, by studying a continuous mathematical model of X-ray tomography, and showing that some properties, determining the solvability of the model carry, over to a discretised version. From this knowledge a method of analysis is defined, to determine the solvability of specific tomography problems. This finally leads to the investigation of *laminar tomography*.

It will become clear, in Chapter 2, what is meant by *solvability*, and what properties are considered to determine the solvability of an X-ray tomography problem.

1.1 Structure of The Thesis

To satisfy the goal we have divided the thesis into two parts; the first part sets the stage and provides the reader with relevant background knowledge required in the thesis. In particular the first part shows that X-ray tomography problems are ill-posed, and it provides tools for analysing ill-posedness in both the continuous and discretised cases of these problems. The second part consists of a systematic analysis of specific X-ray tomography problems based on a method of analysis derived from the relevant theory in the first part.

The thesis is organised as follows:

- *Chapter 2, Sections 2.1-2.3:* Introduces the term ill-posed as a method of determining solvability and shows that the first-kind Fredholm integral equation is ill-posed.
- *Chapter 2, Sections 2.4-2.5:* Introduces the Picard condition as a method of determining how the solution to a specific problem is affected by its ill-posedness.
- *Chapter 2, Sections 2.6-2.7:* Introduces a mathematical way of modelling CT and relates it to the first-kind Fredholm integral equation.
- *Chapter 2, Sections 2.8-2.9:* Introduces the discretised version of CT and shows the ill-posed characteristics of the continuous version carries over.
- *Chapter 3, Section 3.1:* Defines the analysis method used in the second part of the thesis.
- *Chapter 3, Sections 3.2-3.5:* Contains the analysis applied to a number of "toy" problems.
- *Chapter 4:* Contains the analysis applied to two cases of laminar tomography.
- *Chapter 5:* Contains the conclusion of the thesis and a discussion of future work.

Chapter 2

Background Theory

The goal of this chapter is to describe the relevant background theory required to perform an analysis of the solvability of X-ray tomography problems. The chapter will start off by defining inverse problems and some general theory for problems that can be modelled by the Fredholm integral equation of the first kind. Later the theory of X-ray tomography will be introduced and the theory from the first sections of the chapter will be applied to this. The latter part of the chapter will cover the methods and challenges of performing X-ray tomography on a computer. In this chapter the reader is expected to have a profound understanding of linear algebra and be familiar with the basic concepts of real analysis including L^p-spaces and Fourier analysis.

2.1 Inverse Problems

The term *inverse problem* generally tends to describe the framework used in mathematics to gain information about an object or system, that we cannot directly observe. The information is gained by processing measurements of some physical property affected by the object. The goal of solving the inverse problem is then, to find the approximation of the object that best matches the measured property.

A general mathematical statement of an inverse problem is to find the model parameters, f, such that,

$$\mathcal{A}(f) = g. \tag{2.1}$$

Here $\mathcal{A}$ is an operator that describes the relation between the model parameters, f, of the object and some measurements, g. To clarify this; we call the process of constructing g given f the *forward problem* and finding f given g the *inverse problem*. We note that, an X-ray tomography problem can be considered as an inverse problem.

In general, it turns out that these kinds of problems are *ill-posed* [2], [3]. To understand what is meant by ill-posed, we look to the definition given by Hadamard in 1902 [4].

Definition 2.1 A mathematical problem is *well-posed* if it has the following properties

- Existence: A solution to the problem exists.
- Uniqueness: The solution is unique.
- Stability: The solution's behaviour changes *continuously* with initial conditions.

If any of these conditions are not satisfied, the problem is said to be *ill-posed*.

As it turns out ill-posed problems are generally hard to solve, and as we will see in Section 2.3, the question of determining the solvability of X-ray tomography problems demands a closer look at the stability criterion. In this thesis we will therefore focus on analysing this criterion for general and specific X-ray tomography problems. For further detail on the uniqueness and existence criterion see, e.g., [2].

2.2 Notation

Here we define some notation commonly used in the following sections.

We make use of the domain space:

$$\Omega \equiv \{x \in \mathbb{R}^2 \mid \|x\|_2 \leq 1\} \qquad \text{(Unit disc in } \mathbb{R}^2\text{)}.$$

Where $\|\cdot\|_2$ is the usual Euclidean norm in $\mathbb{R}^2$.

We will consider functions on $L^p(\mathbb{R})$-space where $p = 2$ unless stated otherwise. We define the L^p-space for real functions by

$$L^p(\mathbb{R}) \equiv \left\{ f : \mathbb{R} \to \mathbb{R} \;\middle|\; \left(\int_{-\infty}^{\infty} |f(t)|^p \, \mathrm{d}t \right)^{1/p} < \infty \right\}.$$

We define the inner product of the functions $\phi, \psi : \mathbb{R} \to \mathbb{R}$ on $L^2(\mathbb{R})$ by

$$\langle \phi, \psi \rangle \equiv \int_{-\infty}^{\infty} \phi(t)\psi(t) \, \mathrm{d}t,$$

and the norm of ϕ on $L^2(\mathbb{R})$ by

$$\|\phi\| \equiv \langle \phi, \phi \rangle^{1/2} = \left(\int_{-\infty}^{\infty} \phi(t)^2 \, \mathrm{d}t \right)^{1/2}.$$

Remark. Note that any function, $f \in L^2$, is also a function in L^1. Thus any theorems pertaining to functions in L^1 will also hold for functions in L^2.

Additionally, we define $\mathcal{F} : L^1 \to L^1$ as the operator given by the Fourier transform of $f \in L^1(\mathbb{R})$. We let $\hat{f} : \mathbb{R} \to \mathbb{C}$ be the function associated with the Fourier transform such that

$$(\mathcal{F}f)(\gamma) = \hat{f}(\gamma) \equiv \int_{-\infty}^{\infty} f(x) e^{-2\pi \hat{\imath} x \gamma} \, \mathrm{d}x, \gamma \in \mathbb{R}, \tag{2.2}$$

where $\hat{\imath} = \sqrt{-1}$. The inversion formula of the Fourier transform is defined as

$$f(x) = \int_{-\infty}^{\infty} \hat{f}(\gamma) e^{2\pi \hat{\imath} x \gamma} \, \mathrm{d}\gamma \quad \text{for almost all } x \in \mathbb{R},$$

where $f \in L^2(\mathbb{R})$ and $\hat{f} \in L^1(\mathbb{R})$.

We also define $K * f : \mathbb{R} \to \mathbb{C}$ as the convolution of $K, f \in L^1(\mathbb{R})$ by

$$(K * f)(y) \equiv \int_{-\infty}^{\infty} K(y - x) f(x) \, \mathrm{d}x, y \in \mathbb{R}. \tag{2.3}$$

2.3 Ill-Posedness of The First-Kind Fredholm Integral Equation

X-ray tomography belongs to the class of linear inverse problems that can be modelled by the Fredholm integral equation of the first kind. In Section 2.6, we give an intuitive explanation, based on the theory, as to why this is the case. But for now, we will consider some properties found for this integral equation. The first-kind Fredholm integral equation is defined as:

$$\int_{-\infty}^{\infty} K(s,t)f(t)\,\mathrm{d}t = g(s), \qquad s \in \mathbb{R}. \tag{2.4}$$

In the inverse problem the *kernel*, $K \in L^2(\mathbb{R}^2)$, and the right-hand side, $g \in L^2(\mathbb{R})$, are known quantities, and $f \in L^2(\mathbb{R})$ is unknown. From Equation (2.1) we recognise the operator as applying the integral and kernel to the object, f, and likewise g as the measurements. We denote this operator as $\mathcal{K} : L^2(\mathbb{R}) \to L^2(\mathbb{R})$ and define it by

$$(\mathcal{K}f)(s) \equiv \int_{-\infty}^{\infty} K(s,t)f(t)\,\mathrm{d}t = g(s).$$

An important special case of this integral equation is when the kernel is a function of the difference between s and t such that $K(s,t) = K(s-t)$. In this case we recognise that the right hand side g is the *convolution* of f and K, such that;

$$(f * K)(s) = \int_{-\infty}^{\infty} K(s-t)f(t)\,\mathrm{d}t = g(s). \tag{2.5}$$

When solving for f, this version of the integral equation is called a *deconvolution* problem. Going further it will prove sufficient to focus on this specific type of problem. To gain further insight into the nature of the deconvolution problem, we will explain why it is ill-posed. To do this, we must introduce two relevant theorems.

Theorem 2.2 (Riemann-Lebesgue's Lemma) *For $f \in L^1(\mathbb{R})$, $\hat{f}$ is a continuous function which tends to zero as $\gamma \to \pm\infty$.*

The proof of the Riemann-Lebesgue's lemma is omitted in the thesis. The interested reader can seek out [5] (proof starts on page 138). The second theorem will show a useful relation between the convolution operator (2.3) and the Fourier transform (2.2).

Theorem 2.3 (Fourier Transform and Convolution) *If $K, f \in L^1(\mathbb{R})$, then $\widehat{K * f}(\gamma) = \hat{K}(\gamma)\hat{f}(\gamma)$, $\forall\gamma \in \mathbb{R}$.*

Proof. First we note, that for $K, f \in L^1(\mathbb{R})$ the convolution $(K * f) : \mathbb{R} \to \mathbb{C}$ is well defined and defines a function in $L^1(\mathbb{R})$ by Lemma 7.3.2 in [5]. Indeed the Fourier transform of $(K * f)(y)$ is then well defined and given by

$$\begin{aligned}\widehat{K * f}(\gamma) &= \int_{-\infty}^{\infty} (K * f)(y) e^{-2\pi \hat{\imath} y\gamma} \, \mathrm{d}y \\ &= \int_{-\infty}^{\infty} \left(\int_{-\infty}^{\infty} K(y-x) f(x) \, \mathrm{d}x \right) e^{-2\pi \hat{\imath} y\gamma} \, \mathrm{d}y.\end{aligned}$$

Using Fubini's Theorem, Theorem 5.3.10 in [5], we can switch the order of integration, and using the fact that $e^{-2\pi \hat{\imath} y\gamma} = e^{-2\pi \hat{\imath}(y-x)\gamma} e^{-2\pi \hat{\imath} x\gamma}$ we get

$$\begin{aligned}\widehat{K * f}(\gamma) &= \int_{-\infty}^{\infty} \left(\int_{-\infty}^{\infty} K(y-x) e^{-2\pi \hat{\imath} y\gamma} \, \mathrm{d}y \right) f(x) \, \mathrm{d}x \\ &= \int_{-\infty}^{\infty} \left(\int_{-\infty}^{\infty} K(y-x) e^{-2\pi \hat{\imath}(y-x)\gamma} \, \mathrm{d}y \right) f(x) e^{-2\pi \hat{\imath} x\gamma} \, \mathrm{d}x.\end{aligned}$$

Now we see by a simple change of variable, $z = y - x$ such that $\mathrm{d}z = \mathrm{d}x$, the desired result;

$$\begin{aligned}\widehat{K * f}(\gamma) &= \int_{-\infty}^{\infty} \left(\int_{-\infty}^{\infty} K(z) e^{-2\pi \hat{\imath} z\gamma} \, \mathrm{d}z \right) f(x) e^{-2\pi \hat{\imath} x\gamma} \, \mathrm{d}x \\ &= \left(\int_{-\infty}^{\infty} K(z) e^{-2\pi \hat{\imath} z\gamma} \, \mathrm{d}z \right) \left(\int_{-\infty}^{\infty} f(x) e^{-2\pi \hat{\imath} x\gamma} \, \mathrm{d}x \right) \\ &= \widehat{K}(\gamma) \hat{f}(\gamma).\end{aligned}$$

□

Now, to show that the deconvolution problem is ill-posed; we recall that, the stability condition of Definition 2.1 is satisfied if the solutions behaviour changes continuously with initial conditions. Thus the deconvolution problem is ill-posed if a small perturbation, say $\epsilon \in L^2(\mathbb{R})$, in the measurements, g, can lead to an arbitrarily large change in the model parameters, f.

We denote the true model parameters of the object as, $f^0 \in L^2(\mathbb{R})$, and the perturbed measurements as $g_\epsilon(s) = g(s) + \epsilon(s)$. We can then study the effect on the inverse problem caused by perturbing the measurements.

Using the true model parameters, f^0, we can write the perturbed measurements as

$$g_\epsilon(s) = (K * f^0)(s) + \epsilon(s), \tag{2.6}$$

and from the model parameters, $f_\epsilon \in L^2(\mathbb{R})$, found by solving the inverse problem with perturbed measurements as

$$g_\epsilon(s) = (K * f_\epsilon)(s). \tag{2.7}$$

Now using Theorem 2.3 we can then write the Fourier transformation of $g_\epsilon(s)$ in terms of Equations (2.6) and (2.7) by

$$\hat{g}_\epsilon(\gamma) = \widehat{K}(\gamma)\hat{f}_\epsilon(\gamma) = \widehat{K}(\gamma)\hat{f}^0(\gamma) + \hat{\epsilon}(\gamma).$$

Rearranging the equation we find the relation between the Fourier transformation of the true model parameters and the Fourier transformation of f_ϵ as

$$\hat{f}_\epsilon(\gamma) = \hat{f}^0(\gamma) + \frac{\hat{\epsilon}(\gamma)}{\widehat{K}(\gamma)}. \tag{2.8}$$

If we then take the inverse Fourier transformation of Equation (2.8) we get

$$\begin{aligned} f_\epsilon(x) &= \int_{-\infty}^{\infty} \hat{f}_\epsilon(\gamma) e^{2\pi \hat{\imath} x\gamma} \, \mathrm{d}\gamma \\ &= \int_{-\infty}^{\infty} \hat{f}^0(\gamma) e^{2\pi \hat{\imath} x\gamma} \, \mathrm{d}\gamma + \int_{-\infty}^{\infty} \frac{\hat{\epsilon}(\gamma)}{\widehat{K}(\gamma)} e^{2\pi \hat{\imath} x\gamma} \, \mathrm{d}\gamma \\ &= f^0(x) + \int_{-\infty}^{\infty} \frac{\hat{\epsilon}(\gamma)}{\widehat{K}(\gamma)} e^{2\pi \hat{\imath} x\gamma} \, \mathrm{d}\gamma. \end{aligned}$$

We recognise the second part of the equation as the change in the model parameters caused by the perturbations in the measurements. Thus, given small but sufficiently high frequent perturbations (read: noise) in the measurements, we can get arbitrarily large changes in the model parameters. See pages 8-9 in [2] for examples of this behaviour on a few simple problems.

The consequence of this, is that inverse problems on the form in Equation (2.5), do not satisfy the third condition of Definition 2.1, and are therefore ill-posed. But is it possible to identify those elements of the deconvolution problem that contribute to this behaviour? If so; we could perhaps, by treating these, end up with reasonable estimates of model parameters even with noise in measurements. A tool to quantify this behaviour is the singular value expansion.

2.4 Singular Value Expansion

The singular value expansion (SVE) provides a method for describing the behaviour of inverse problems by considering the frequency components of the transformation. This will indeed prove useful for identifying components of the deconvolution problem that contribute to its ill-posedness. Before we get ahead of ourselves, we must first state the definition of the SVE.

Definition 2.4 (Singular Value Expansion) Let $K \in L^2(\mathbb{R}^2)$ be a square integrable function and let $u_i : \mathbb{R} \to \mathbb{R}$ and $v_i : \mathbb{R} \to \mathbb{R}$ be orthonormal functions in $L^2(\mathbb{R})$ such that

$$\langle u_i, u_j \rangle = \langle v_i, v_j \rangle = \delta_{ij} \text{ for } i, j \in \mathbb{N},$$

and $\{\mu_i\}_{i=1}^{\infty}$ be a non-increasing sequence such that $\mu_1 \geq \mu_2 \geq \cdots \geq 0$. Then the *singular value expansion* of K are the functions, u_i, v_i, and values, μ_i, that satisfy

$$K(s,t) \equiv \sum_{i=1}^{\infty} \mu_i u_i(s) v_i(t).$$

Here the functions u_i and v_i are called the left and right singular functions respectively, and μ_i are called the singular values of K.

Remark. It is relevant to note that the singular functions, u_i and v_i, form an orthonormal basis in $L^2(\mathbb{R})$. This is clear from the definition of an orthonormal system – see, e.g., Definition 4.3.1 and 4.7.1 in [5].

It will become clear later, how to use the SVE for identifying the *ill-posed parts* of the deconvolution problem. However, first we describe an important relation that the singular functions and values satisfy. In fact it is named "*the fundamental relation*".

Theorem 2.5 (The Fundamental Relation of the SVE) *Let u_i and v_i be the singular functions of some kernel $K \in L^2(\mathbb{R}^2)$, and let μ_i be the singular values of the same kernel such that they satisfy Definition 2.4. Then we have the fundamental relation*

$$\int_{-\infty}^{\infty} K(s,t) v_i(t) \, \mathrm{d}t = \mu_i u_i(s), \qquad i = 1, 2, \ldots \quad .$$

Proof. By the definition of an inner product in L^2 and from the SVE of K we have that

$$\begin{aligned}\int_{-\infty}^{\infty} K(s,t)v_i(t)\,\mathrm{d}t &= \langle K(s,t), v_i(t)\rangle \\ &= \left\langle \sum_{j=1}^{\infty} \mu_j u_j(s) v_j(t), v_i(t) \right\rangle \\ &= \sum_{j=1}^{\infty} \mu_j u_j(s) \left\langle v_j(t), v_i(t)\right\rangle .\end{aligned}$$

Since v is an orthonormal basis for $L^2(\mathbb{R})$ such that $\langle v_j, v_i\rangle = 1$ only for $i = j$ and zero otherwise, we get the desired result;

$$\int_{-\infty}^{\infty} K(s,t)v_i(t)\,\mathrm{d}t = \mu_i u_i(s).$$

□

From this relation one can find a number of properties for the SVE of K. We will focus on one of these properties, namely the Picard condition, which is the final ingredient we need to distinguish the components that are dominated by high frequent perturbations in measurements, from those that are not.

2.5 The Picard Condition

Before stating the Picard condition, we recall that u_i and v_i form bases for square integrable functions in $L^2(\mathbb{R})$, and thus, by the characterisation of orthonormal bases – see, e.g., Theorem 4.7.2 b in [5] – we can expand both f and g in terms of these basis functions:

$$f(t) = \sum_{i=1}^{\infty} \langle v_i, f\rangle\, v_i(t), \qquad g(s) = \sum_{i=1}^{\infty} \langle u_i, g\rangle\, u_i(s). \tag{2.9}$$

Using the above expansions, we can write the first-kind Fredholm integral equation (2.4) as

$$\int_{-\infty}^{\infty} K(s,t) \sum_{i=1}^{\infty} \langle v_i, f\rangle\, v_i(t)\,\mathrm{d}t = \sum_{i=1}^{\infty} \langle u_i, g\rangle\, u_i(s), \tag{2.10}$$

and then applying the fundamental relation of the SVE, in Theorem 2.5, we are able to write the left-hand side as

$$\begin{aligned}\int_{-\infty}^{\infty} K(s,t) \sum_{i=1}^{\infty} \langle v_i, f\rangle \, v_i(t) \, \mathrm{d}t &= \left\langle K(s,t) \sum_{i=1}^{\infty} \langle v_i, f\rangle \, , v_i(t) \right\rangle \\ &= \sum_{i=1}^{\infty} \langle v_i, f\rangle \, \langle K(s,t), v_i(t)\rangle \\ &= \sum_{i=1}^{\infty} \langle v_i, f\rangle \, \mu_i u_i(s).\end{aligned}$$

and applying this in Equation (2.10) and dividing by μ_i, we get that

$$\sum_{i=1}^{\infty} \langle v_i, f\rangle \, u_i(s) = \sum_{i=1}^{\infty} \frac{\langle u_i, g\rangle}{\mu_i} u_i(s). \tag{2.11}$$

We will use this result in the proof of the Picard condition.

Theorem 2.6 (The Picard condition) *Let u_i be the left singular functions and μ_i the singular values from the SVE of K in Definition 2.4. Then the solution, f, to the inverse problem of Equation (2.4) is square integrable if*

$$\sum_{i=1}^{\infty} \left(\frac{\langle u_i, g\rangle}{\mu_i} \right)^2 < \infty.$$

Proof. For f to be square integrable we require $\|f\|^2 = \int_{-\infty}^{\infty} f(t)^2 \, \mathrm{d}t < \infty$. But since $\int_{-\infty}^{\infty} f(t)^2 \, \mathrm{d}t = \langle f, f\rangle$ by definition, we can use the expansion of f, in Equation (2.9), and the first property of the inner product space (see, e.g., Definition 4.1.1 in [5]) to write

$$\langle f, f\rangle = \left\langle \sum_{i=1}^{\infty} \langle v_i, f\rangle \, v_i, f \right\rangle = \sum_{i=1}^{\infty} \langle v_i, f\rangle^2 .$$

Then by realising that, the expansion coefficients for u_i, in Equation (2.11), must be equal in each term, we find $\langle v_i, f\rangle = \frac{\langle u_i, g\rangle}{\mu_i}$, which yields the desired result that the solution is square integrable if

$$\|f\|_2^2 = \sum_{i=1}^{\infty} \langle v_i, f\rangle^2 = \sum_{i=1}^{\infty} \left(\frac{\langle u_i, g\rangle}{\mu_i} \right)^2 < \infty.$$

□

The Picard condition gives us a tool to check, if our deconvolution problem is dominated by high frequent perturbations in measurements, such that the model parameters are no longer square integrable. A general assumption on real world data is that, it is square integrable. Hence, we cannot expect solutions to be meaningful, if the Picard condition is not satisfied. We note that the ill-posedness depend on the size of the singular values μ_i, since $\frac{\langle u_i, g \rangle}{\mu_i} \to \infty$ for $\mu_i \to 0$.

Remark. (Spectral Characterization of the Singular Functions) The singular functions, u_i and v_i, are similar to the Fourier functions in the sense that for large singular values the corresponding singular functions are low frequent and for small singular values the corresponding functions are high frequent. See pages 17-20 in [2] for a justification of this.

2.6 Computed Tomography

Returning to X-ray tomography problems: It is in this section, we justify that they can be modelled by the deconvolution problem, in Equation (2.5). Because of this, we can use the results from the previous theory on X-ray tomography problems. To start with, a proper introduction of the problem is in its place.

In X-ray tomography, we measure the intensity loss of an X-ray beam going through an object. The beam originates from a source with initial intensity, I_0, and finishes at a detector with damped intensity, I. The loss of intensity is due to the energy absorption by the object, which depend on its structure. The beam goes through the object in a straight line, $\mathbb{L}$, with an intensity at each point, $I(x)$, for $x \in \mathbb{L}$.

We can describe the loss of the beams intensity on a infinitesimally small part of the line, $\mathrm{d}l$, from how the structure of the object, described by the true model parameters, f^0, absorbs this intensity. We can write this as

$$\mathrm{d}I(x) = -f^0(x)I(x)\ \mathrm{d}l,$$

which can be rewritten as

$$\begin{aligned} \frac{1}{I(x)}\frac{\mathrm{d}I(x)}{\mathrm{d}l} &= -f^0(x) \\ \int_{\mathbb{L}} \frac{1}{I(x)}\frac{\mathrm{d}I}{\mathrm{d}l}\ \mathrm{d}l &= \int_{\mathbb{L}} -f^0(x)\ \mathrm{d}l \\ -\ln\left(\frac{I}{I_0}\right) &= \int_{\mathbb{L}} f^0(x)\ \mathrm{d}l. \end{aligned}$$

From this, we are now able to describe the integral of f^0 over the line, $\mathbb{L}$, by measuring the initial and damped intensity. In further notation, we will call this integral a *projection*, $p(\mathbb{L})$, given by

$$p(\mathbb{L}) = \int_{\mathbb{L}} f^0(x) \, \mathrm{d}l. \tag{2.12}$$

We can recognise the above equation as a first-kind Fredholm integral equation – see Equation (2.4) – if the kernel K describes how we integrate over the line, $\mathbb{L}$. If this kernel can be written as a function of the difference between its arguments, we discover the deconvolution problem. In the next section we will study the most common way of further formulating Equation (2.12).

2.7 The Radon Transform in Two Dimensions

The Radon transform, $\mathcal{R}$, due to Johann Radon in 1917 [6], is a central example of formulating X-ray tomography on the form in Equation (2.12). We note that, in two dimensions f is now a function of two variables. The variables describe the position of a point, (x_1, x_2), in a two dimensional image. We will later give an intuitive explanation of how to understand this two dimensional problem in terms of the earlier theory.

By writing the line, $\mathbb{L}$, as a function of the angle, θ, and the distance, s, as shown in Figure 2.1, we find, the set of points that make up $\mathbb{L}$ can be characterized as

$$\mathbb{L}(s, \theta) = \{(x_1, x_2) \in \mathbb{R}^2 \mid x_1 \cos\theta + x_2 \sin\theta = s\}. \tag{2.13}$$

Where $\theta \in [0, \pi[$ is the slope of the line going through the origin orthogonal to $\mathbb{L}$ and $s \in \mathbb{R}$ is the distance between the origin and the line, $\mathbb{L}$, see Figure 2.1.

If we plug this into Equation (2.12), using a Dirac delta function to integrate over the line, $\mathbb{L}$, we find what is known as the Radon transform.

Definition 2.7 (The Radon Transform) Let $f^0 : \mathbb{R}^2 \to \mathbb{R}$ be a square integrable and compactly supported function describing the model parameters of an object and let $\mathbb{L}$ be the line given by Equation (2.13), then the Radon transform, $\mathcal{R}$, of f^0 is defined as:

$$(\mathcal{R}f^0)(s, \theta) \equiv \int_{-\infty}^{\infty} \int_{-\infty}^{\infty} f^0(x_1, x_2) \delta(x_1 \cos\theta + x_2 \sin\theta - s) \mathrm{d}x_1 \mathrm{d}x_2. \tag{2.14}$$

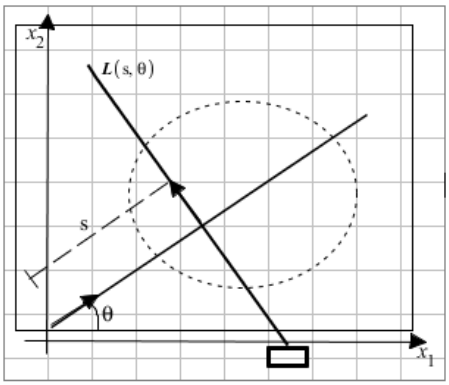

Figure 2.1: Illustration of the line $\mathbb{L}(s,\theta)$.

Remark. The complete set of projections, for all θ, of the Radon transform is referred to as the sinogram of f^0.

By change of variable $x_1 = \frac{x}{\cos\theta}$, such that $\mathrm{d}x_1 = \frac{\mathrm{d}x}{\cos\theta}$, and using the property of the delta function we can write the Radon transform as

$$\begin{aligned}(\mathcal{R}f^0)(s,\theta) &= \int_{-\infty}^{\infty}\int_{-\infty}^{\infty} f^0(\frac{x}{\cos\theta}, x_2)\delta(x + x_2\sin\theta - s)\frac{1}{\cos\theta}\mathrm{d}x\mathrm{d}x_2 \\ &= \int_{-\infty}^{\infty} f^0(\frac{-x_2\sin\theta + s}{\cos\theta}, x_2)\frac{1}{\cos\theta}\mathrm{d}x_2.\end{aligned}$$

Changing variable $x_2 = s\sin\theta + l\cos\theta$, such that $\mathrm{d}x_2 = \cos\theta\mathrm{d}l$, we get

$$\begin{aligned}(\mathcal{R}f^0)(s,\theta) &= \int_{-\infty}^{\infty} f^0\left(\frac{-(s\sin\theta + l\cos\theta)\sin\theta + s}{\cos\theta}, s\sin\theta + l\cos\theta\right)\mathrm{d}l \\ &= \int_{-\infty}^{\infty} f^0\left(\frac{s(-\sin\theta^2 + 1)}{\cos\theta} - l\sin\theta, s\sin\theta + l\cos\theta\right)\mathrm{d}l \\ &= \int_{-\infty}^{\infty} f^0\left(s\cos\theta - l\sin\theta, s\sin\theta + l\cos\theta\right)\mathrm{d}l.\end{aligned}$$

We now recognise the values of $(\mathcal{R}f^0)$ for fixed θ as the projection defined in Equation (2.12). We denote this projection as $p_\theta(s)$ and write it as

$$p_\theta(s) = \int_{\mathbb{L}(s,\theta)} f^0(x)\ \mathrm{d}l.$$

As we saw in the last part of the previous section, the projection, $p(\mathbb{L})$, could be written as a first-kind Fredholm integral equation. We expect the same to

be true of the Radon transform for fixed θ, since $p_\theta(s)$ has the same form as $p(\mathbb{L})$, in Equation (2.12).

We note that the kernel, K, describes the nature of the integral transform for the first-kind Fredholm integral equation (2.4). Since the Dirac delta function, $\delta \notin L^2(\mathbb{R}^2)$, has the same property for the Radon transform as seen, in Equation (2.14), we can with slight abuse of notation compare the two.

When doing this comparison, we see that the delta function acts like the kernel for the deconvolution problem, in Equation (2.5), and thus we expect the theory of ill-posedness to hold true for the Radon transform. A more rigorous analysis of this proposition could be an interesting future project.

It turns out that the operator for the Radon transform is unbounded on $L^2(\mathbb{R}^n)$, but is bounded for some weighted L^2-spaces, by Theorem 2.9 in [7], as well as for L^1-spaces. To further justify the theory of ill-posedness for the Radon transform, we can consider the singular values from the SVE of the Radon transform on a unit disc, $\mathcal{R}(\Omega)$, which Bertero [3] and Frikel [7] explains, now maps to a weighted L^2-space.

Theorem 2.8 *The singular values of the Radon transform, $\mathcal{R}(\Omega)$, is given by*

$$\mu_m = \left(\frac{4\pi}{m+1}\right)^{1/2},$$

where μ_m has multiplicity m and is ordered in a non-increasing fashion such that the set of singular values is $\{\mu_1, \mu_2, \mu_2, \mu_3, \mu_3, \mu_3, \ldots\}$.

The proof of this theorem can be found in [3].

2.8 Discretisation

For the inverse problem we have in Section 2.7 assumed infinitely many projections available for the reconstruction of the model parameters from the object. However, this is not the case in computed X-ray tomography where a detector can only measure a finite number of projections. Additionally, computers are not well equipped to solve problems on continuous domains, so in practice one will have to discretise the domain, such that the reconstruction can be calculated and stored on a computer. Hence, we are motivated to investigate the properties of the discretised X-ray tomography problems.

When considering X-ray tomography problems the object is almost always represented as an image. The model parameters then describes the intensity of each point in the image. By the assumption that, in the continuous version of the object, points in a neighbourhood of each other will be closely related, we can approximate the object by discretisation. Then we will have a vector, $\mathbf{x} \in \mathbb{R}^{1\times n}$, describing the object, where n is the number of pixels. An example of a discretised object with a single projection going through can be seen in Figure 2.2.

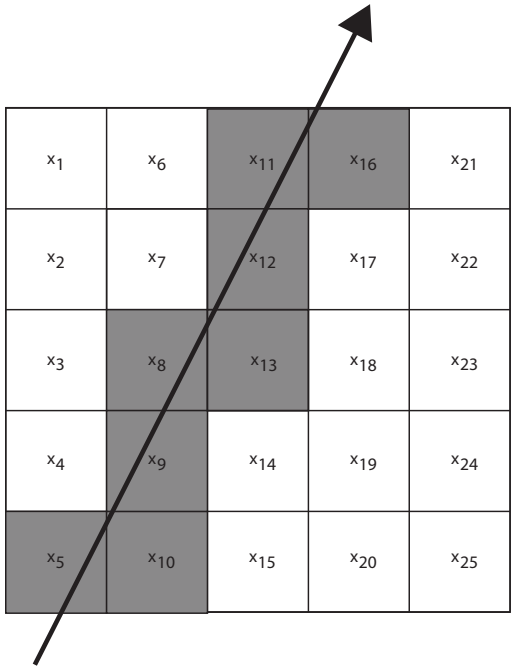

Figure 2.2: Discretised object with $n = 25$ pixels

By discretising, we are able to represent each line going through the object by the length it travels through each pixel. We store these lengths for each line, $\mathbb{L}_i$, in a row vector, $\mathbf{a}_i \in \mathbb{R}^n$, where i is the index distinguishing between the different lines. By doing this, we are able to approximate the projection over the ith line as

$$p(\mathbb{L}_i) = \int_{\mathbb{L}_i} f^0(x)\,\mathrm{d}x \approx \sum_{j=1}^{n} a_{ij}x_j,$$

where $a_{i,j}$ is the jth element of $\mathbf{a}_i$ and x_j is the jth pixel value of the object $\mathbf{x}$. By collecting all the lines expressed as row vectors into one matrix we get

$$A = \begin{pmatrix} \mathbf{a}_1 \\ \mathbf{a}_2 \\ \vdots \\ \mathbf{a}_m \end{pmatrix},$$

where m is the number of lines and $A \in \mathbb{R}^{m\times n}$. We are now able to compute the approximated sinogram, $\mathbf{b}$, of the linear system as

$$A\mathbf{x} = \mathbf{b}. \tag{2.15}$$

Using a computer, this approximated sinogram is easily computed compared to the continuous sinogram, e.g., for the Radon transform in Equation (2.14). If we are looking at the inverse problem, we solve Equation (2.15) for $\mathbf{x}$. To investigate this problem further, we first consider what changes due to the discretisation. The object, $\mathbf{x}$, is now in $\mathbb{R}^n$ and the measurements or sinogram, $\mathbf{b}$, is in $\mathbb{R}^m$. Then we have the transformation matrix $A : \mathbb{R}^n \to \mathbb{R}^m$, which represents the forward problem.

Remark. The bright reader might ask if A is well defined without a weighting on the discrete sinogram space, since $\mathcal{R}$ was unbounded mapping into $L^2(\mathbb{R})$. This is a very good question and it is studied in [3], where Bertero explains that a change of variables, based on the Choleski factorization of the weighting matrices allows one to transform a problem formulated in weighted spaces into a problem formulated in canonical vector spaces. The explanation of why this is true is out of the scope of this thesis.

In the discretised spaces, we will use the commonly used norms:

$$\|\mathbf{x}\| = \left(\sum_{i=1}^{n} x_i^2\right)^{1/2} \qquad \text{for } \mathbf{x} \in \mathbb{R}^n$$
$$\|\mathbf{b}\| = \left(\sum_{i=1}^{m} b_i^2\right)^{1/2} \qquad \text{for } \mathbf{b} \in \mathbb{R}^m.$$

Now that the normed spaces are defined, we investigate the properties of the system, in Equation (2.15). From Section 2.7 we know that the inverse problem of the Radon transformation does not satisfy the third condition of Definition 2.1, and is thus ill-posed. However, in the discrete case, checking continuity is useless since every map from a discrete domain is continuous. The discrete inverse problem of Equation (2.15) is hence well-posed if $\text{Rank}(A) = n = m$. This is true since there exist one unique solution and the solution depends continuously on the data. So the stability condition from Definition 2.1 is not a good way of describing stability of linear systems on the form 2.15.

Instead we must consider if the system is *ill-conditioned*. Ill-conditioned means small perturbations in the data will reflect dramatically on the reconstruction of the object. We describe ill-conditionedness by how the perturbations propagate through to the solution in the inverse problem.

If $\mathbf{b}_\varepsilon = \mathbf{b} + \varepsilon$ is the sinogram with perturbation $\varepsilon \in \mathbb{R}^m$, then let $\mathbf{x}_\varepsilon$ be the solution to the system $A\mathbf{x}_\varepsilon = \mathbf{b}_\varepsilon$. We can then investigate the error propagation from the measurements to the solution. The reflection made by this perturbation can be described by the following relation:

$$\frac{\|\mathbf{x}_\varepsilon\|}{\|\mathbf{x}\|} \leq C_A \frac{\|\mathbf{b}_\varepsilon\|}{\|\mathbf{b}\|}.$$

Here C_A is the condition number as defined below.

Definition 2.9 The condition number, C_A, of a given transformation matrix A, satisfying equation (2.15), is given by

$$C_A = \|A^{-1}\|\|A\|.$$

Here the norm of the matrix, A, is defined as $\|A\| \equiv \max_{\mathbf{x}\neq 0}\left\{\frac{\|A\mathbf{x}\|}{\|\mathbf{x}\|}\right\}$.

It should be mentioned that this restriction is pessimistic and in many cases, the reflection is much smaller than this relation. It gives us an upper bound

for the influence on the reconstruction due to the perturbation of the sinogram. For large matrices, it is easily seen that the condition number can be very large and the system in Equation (2.15) will then be ill-conditioned. Since the upper bound given by the condition number is a weak restriction and Definition 2.9 requires the inverse of A, we are in dire need of more robust tools to study the "ill-posedness" of the discretised problem. We obtain these tools by generalising the analysis of the SVE to the discrete case.

Remark. Perturbation in the measurements, $\mathbf{b}$, for real life X-ray tomography problems is caused by noise from two main sources; either, small obstacles not included in the object or measurement errors caused by the uncertainty of measuring equipment. In this thesis we will consider the perturbation as stochastic and it will be approximated by a Gaussian distribution.

2.9 Singular Value Decomposition and The Discrete Picard Condition

Previously in this chapter, the SVE proved to be a very useful tool for analysing the properties of the first-kind Fredholm integral equation and by Section 2.7 also for the Radon transform. We have a similar tool for the problems described in the discrete space and we will see that most the previously described properties carry over. This tool is called *the singular value decomposition* (SVD).

Definition 2.10 Let $A \in \mathbb{R}^{m\times n}$, satisfy Equation (2.15), then there exist a diagonal matrix, $\Sigma \in \mathbb{R}^{m\times n}$, with non negative diagonal elements, and two square orthogonal matrices $U \in \mathbb{R}^{m\times m}$ and $V \in \mathbb{R}^{n\times n}$ such that

$$A = U\Sigma V^T = \sum_{i=1}^{r} \mathbf{u}_i \sigma_i \mathbf{v}_i^T,$$

where $V^T \in \mathbb{R}^{n\times n}$ is the transposed V and $r = \text{Rank}(A)$.

Remark. For complex matrices we would have to use V^*, the adjoint of V, instead of V^T.

The matrices U and V consist of what is known as the singular vectors $\mathbf{u}_i \in \mathbb{R}^m$ and $\mathbf{v}_i \in \mathbb{R}^n$, such that

$$U = (\mathbf{u}_1, \mathbf{u}_2, \mathbf{u}_3, \mathbf{u}_4, \ldots, \mathbf{u}_m), \quad V = (\mathbf{v}_1, \mathbf{v}_2, \mathbf{v}_3, \mathbf{v}_4, \ldots, \mathbf{v}_n),$$

and since they are orthogonal,

$$U^T U = UU^T = \mathbf{I} \text{ and } V^T V = VV^T = \mathbf{I},$$

where $\mathbf{I}$ is the identity matrix.

The diagonal elements of Σ are known as the singular values and are denoted as $\Sigma_{i,i} = \sigma_i$ for $i = 1 \dots \min(m, n)$. For $r = \text{Rank}(A)$ the order of the elements in Σ is as follows $\sigma_1 \geq \sigma_2 \geq ... \geq \sigma_r > 0 = \sigma_{r+1} = \cdots = \sigma_{\min(m,n)}$.

We use the SVD from Definition 2.10 to express the norm of the transformation matrix, A, by its largest singular value:

$$\|A\| = \sigma_1.$$

The derivation of this result is omitted in the thesis.

Remark. We recognise the range, and null space of A as

$$\begin{aligned} \text{Range}(A) &\equiv \{\mathbf{y} \in \mathbb{R}^m \mid \mathbf{y} = A\mathbf{x},\ \mathbf{x} \in \mathbb{R}^n\} \\ &= \text{span}\{\mathbf{u}_i \mid i = 1, 2, \dots, r\} \end{aligned}$$

$$\begin{aligned} \text{Nullspace}(A) &\equiv \{\mathbf{x} \in \mathbb{R}^n \mid A\mathbf{x} = 0\} \\ &= \text{span}\{\mathbf{v}_i \mid i = r+1, r+2, \dots, \min(n, m)\}. \end{aligned}$$

Using Definition 2.10, we can write the solution, $\mathbf{x}$, to the inverse problem of Equation (2.15) as

$$\mathbf{x} = A^{-1}\mathbf{b} = V\Sigma^{-1}U^T\mathbf{b},$$

realising that the inverse of A can be written as

$$A^{-1} = V\Sigma^{-1}U^T.$$

Hence, we observe that the norm of the inverse transformation matrix is given by $\|A^{-1}\| = \sigma^{-1}_{\min\{m,n\}}$. With this remark we are able to express the condition number of A, from Definition 2.9, with help from the SVD by

$$C_A = \|A^{-1}\|\|A\| = \frac{\sigma_1}{\sigma_{\min\{n,m\}}}.$$

This illustrates that the ill-conditionedness of the transformation matrix, A, depends on its singular values, σ_i, like we observed for the ill-posedness of the kernel, K, in Section 2.4.

The singular values from the SVD have a lot of relations which are similar to those from the SVE. We have, e.g., the *fundamental relation*:

$$A\mathbf{v}_i = \sigma_i \mathbf{u}_i, \quad i = 1, \ldots, \min\{n, m\},$$

and if $\text{Rank}(A) = m$ then

$$A^{-1}\mathbf{u}_i = \sigma_i^{-1}\mathbf{v}_i, \quad i = 1, \ldots, \min\{n, m\}.$$

Like we did for the continuous analysis, we can approximate $\mathbf{x}$ in terms of its right singular vectors, $\mathbf{v}_i$, by

$$\mathbf{x} = \mathbf{V}\mathbf{V}^T\mathbf{x} = \sum_{i=1}^{n} (\mathbf{v}_i^T\mathbf{x})\mathbf{v}_i \tag{2.16}$$

and the measurements, $\mathbf{b}$, in terms of the left singular vectors, $\mathbf{u}_i$, by

$$\mathbf{b} = \sum_{i=1}^{r} (\mathbf{u}_i^T\mathbf{b})\mathbf{u}_i. \tag{2.17}$$

The limit, in Equation (2.17), is $r = \text{Rank}(A)$, since we from, Remark 2.9, have that $\mathbf{b} \in \text{Range}(A)$, which is only spanned by the first r left singular vectors.

From the SVD of A and Equation (2.16), we then obtain that

$$A\mathbf{x} = \sum_{i=1}^{r} \mathbf{u}_i \sigma_i \mathbf{v}_i^T (\mathbf{v}_i^T\mathbf{x})\mathbf{v}_i = \sum_{j=1}^{r} \sigma_i (\mathbf{v}_i^T\mathbf{x})\mathbf{u}_i, \tag{2.18}$$

Equating Equation (2.18) and (2.17), we find what is often called the *naive solution* to the inverse problem, of the system in Equation (2.15), as

$$\mathbf{x} = A^{-1}\mathbf{b} = \sum_{i=1}^{r} \frac{\mathbf{u}_i^T\mathbf{b}}{\sigma_i}\mathbf{v}_i. \tag{2.19}$$

Following the same token as for the continuous analysis we want to identify which elements of the transformation matrix, A, will be dominated by noise in the measurements, $\mathbf{b}$, when solving the inverse problem. It is clear from Equation (2.19) that singular values close to zero can have a big impact on the solution from small perturbations in the measurements. Thus, we want to exclude the parts of the sum where the singular values are too small. This leads us to the discrete Picard condition.

Theorem 2.11 (The Discrete Picard Condition - DPC) *Let τ denote the level at which the computed singular values, σ_i, level off due to rounding errors. The DPC is satisfied if, for all singular values larger than τ, the correspondence coefficients, $\|\mathbf{u}_i^T\mathbf{b}\|$, on average, decay faster than the σ_i.*

The relation between the discrete Picard condition and continuous Picard condition is described in detail both in [8] and [2]. We have decided not to include the details of the explanation. However, the important point is that both the singular values and vectors of the SVD can approximate those from the SVE given a sufficiently fine discretisation. For the singular values, σ_i, of the SVD and singular values, μ_i, of the SVE we have the following relation:

$$\sigma_i^{(n)} \leq \sigma_i^{(n+1)} \leq \mu_i, \qquad i = 1, \ldots, n.$$

where n is the number of elements in the discretised object $\mathbf{x}$.

In practical terms the DPC tells us for which index of the singular values the naive solution, in Equation (2.19), start to become dominated by noise in measurements. Thus, to get a better reconstruction than that of the naive solution, we only want to include parts of the sum up until, the index for which the DPC is no longer satisfied. This leads us to define a reconstruction method from truncating the naive solution. This is the well known *truncated singular value decomposition* (TSVD) method. The method is defined in Appendix A together with the Landweber iterative method, and both are used to consider reconstructions in the following chapters.

Chapter 3

SVD Analysis of Interesting Cases

In this Chapter we develop a method for analysing discretised inverse problems. In real world scenarios you often come across problems with data which is not *ideal*. By ideal data we mean sufficiently many, equally distributed, sets of projections from angles all around an object, as shown on figure 3.1.

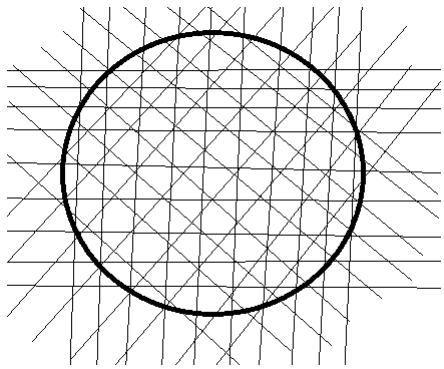

Figure 3.1: Ideal data where we have sets of projections from angles all around the object.

Remark. We note that the word *angles* can be used interchangably with the phrase "sets of projections", since only one set of projections is collected per angle.

For not ideal data, we are then lacking sufficiently many projections or the angles (sets of projections) are not equally distributed around the object. To illuminate what these kind of problems could be like, here are some examples from real world problems: An example could be neutrino tomography, where the projections are collected from random angles. This leads to missing order in the structure of the data, which might lead to complications for the reconstruction. Another example, which we later will investigate closely, could be found in the industrial setting, where we examine objects too long to collect sets of projections from a full angular range, $[0, 179]$ degrees. This leads to a collection of different problems involving missing data and "difficult" discretisation. To study the difficulties of these problems, we will need a method to analyse them with our earlier gathered knowledge from Chapter 2.

3.1 The Analysis Method

The goal of this section is to describe an analysis method in such a way that a person without much knowledge of the theoretical background explained in Chapter 2 can apply it for analysing tomographic problems in practise. From Section 2.4 we saw that the ill-posedness of the inverse problem is dependent on the decay of the singular values from the SVE. Since tomographic problems are usually dealt with on a computer, the SVD is easier computed. Luckily, we know from Section 2.9 that the behaviour of the SVD is a reflection of the one of the SVE. Therefore in further analysis, we will look at the discretised problem.

From Equation 2.16 we know that the object/image $\mathbf{x}$ can be constructed as a linear combination of the right singular vectors $\mathbf{v}_i$. In our analysis we will therefore take a look at what the structure of these vectors can tell us about the reconstructions. To find the singular vectors that are dominated by a realistic noise level, we will use the discrete Picard condition (DPC), defined in Theorem 2.11. We then have the elements of our analysis:

Analysis Method 3.1 *Given a transformation matrix $A \in \mathbb{R}^{m\times n}$ and a sinogram $\mathbf{b} \in \mathbb{R}^m$ s.t. the system is given by $A\mathbf{x} = \mathbf{b}$ where $\mathbf{x} \in \mathbb{R}^n$ is the unknown object we want to reconstruct. We can analyse the system as follows*

- *Calculate the SVD of the transformation matrix A. Then check the decay of the singular values by plotting $\frac{\sigma_i}{\sigma_1}$ compared to the index i.*
- *Check how many of the singular values, σ_i, and corresponding left singular vectors, $\mathbf{u}_i$, satisfy the discrete Picard condition from 2.11.*
- *Analyse the structure of right singular vectors, $\mathbf{v}_i$, of A and check whether it is possible to make a prediction about the reconstruction.*

Additionally, given some supposed representation of $\mathbf{x} \in \mathbb{R}^n$

- *Consider which elements of $\mathbf{x}$ are in the range of A. This gives an idea of what is possible to reconstruct. Likewise considering the null space gives an idea of which elements are not possible to reconstruct.*

So in summary, this analysis method will provide us with insight into how the system is affected by measurement noise, and how the structure of the system can affect the reconstruction. To confirm the assessment in our analysis, we will consider two well known reconstruction techniques, TSVD and Landweber. Throughout the thesis, we will use the well known *Shepp-Logan Phantom*, shown in Figure 3.2.

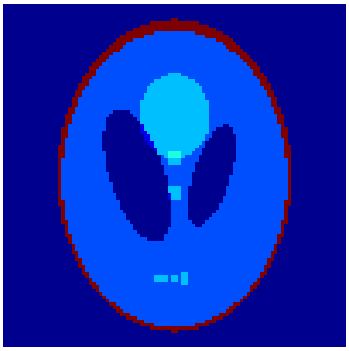

Figure 3.2: A 100×100 Shepp-Logan phantom

When investigating the discrete Picard condition, we will add a relative noise level of $\eta = 5\%$, such that

$$\mathbf{b} = \mathbf{b}_{\text{exact}} + \eta \|\mathbf{b}_{\text{exact}}\| \mathbf{e},$$

where $\mathbf{e}$ is a $1 \times m$ vector with normed Gaussian noise such that $\|\mathbf{e}\| = 1$. It can be used for other objects and noise levels, but we will throughout this thesis consider these choices.

Throughout this thesis, we use Matlab to perform the numerical computations. The script `main.m` consist of all the different set-ups treated in this thesis. The file can be found here [9]. In all of them, we use `analysisSVD.m` to perform the analysis above. The function is described in the list of Matlab functions in the Appendix. Now that we have a method of analysis, we can use it on different tomographic problems. We will start by using our method to motivate a general way to construct the transformation matrix. while motivating the matrix generator, we will show how to use our analysis in more details. Hence, to get a feeling for using the analysis, the reader should go through the next section, even if the subject of consideration is not of particular interest.

3.2 Motivated Choice of Transformation Matrix Generator

To simulate the process of tomographic imaging, one must generate a transformation matrix A, that, together with a test image $\mathbf{x}$, can generate a sinogram or measurements, $\mathbf{b}$. The goal is to find a transformation with a finite number of angles that matches the analytic Radon transform as closely as possible. Two obvious choices come to mind: One extracted from Matlabs own `radon.m` and the one constructed by `paralleltomo.m` from the toolbox AIR Tools [10]. We know the singular values for the analytical Radon transform, $\mathcal{R}(\Omega)$, by Theorem 2.8. Hence, an obvious test of the two transformation matrices would be to see how well they mimic $\mathcal{R}(\Omega)$. We will use our analysis method to study the relation of the two discrete transformations with $\mathcal{R}(\Omega)$.

Before doing so, we note that the transformation matrices from `paralleltomo.m` and `radon.m` correspond to systems in square $N \times N$ domains, such that the objects are vectors in $\mathbb{R}^{N^2}$. Since the singular values from $\mathcal{R}(\Omega)$ are obtained on a unit disc, we must change the domain of these methods into a circular domain and then scale it to a unit circle. We can do this by creating a *mask* and multiplying it element-wise with the transformation matrices. We construct the $\mathbf{mask} \in \mathbb{R}^{N^2}$ with ones inside and zeros outside a disc with diameter N, see Figure 3.3. If we element wise multiply $\mathbf{mask}$ with each row of the transformation

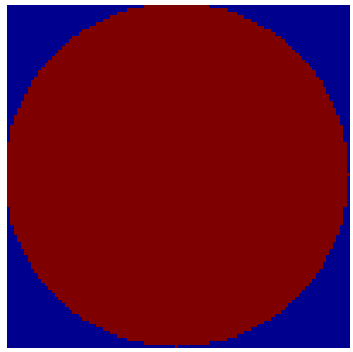

Figure 3.3: Reshaped mask with axes of size $\sqrt{n} = N$, where the value in the blue pixels is zero and one in the red pixels.

matrix, A, we get the transformation matrix for the masked domain. Since the diameter of the discrete domain is N times bigger than the continuous domain, we will multiply the masked transformation matrix with $1/N$ before calculating the SVD. The script `changeDomain_unitcircle.m` makes this change from a square domain into a unit sized circular one.

Throughout this section, we will use $N = 100$ and sets of projections of size $\sqrt{2}N$. The angular range will be $[0, 179]$ with sets of projections sent from every third degree and for `paralleltomo.m` a detector of size $d = \sqrt{2}N$. `radon.m` chooses its own detector size sufficient to compute the projection at unit intervals, even along the diagonal.

Since we have the luxury of actually knowing the true singular values for $\mathcal{R}(\Omega)$, we can test if the singular values from the transformation matrices above satisfy Equation 2.9. In Figure 3.4, we observe that both the matrices' singular values satisfy Equation 2.9 for this example of size and the same is applicable for all other sizes we have tested. Now we want to use our analysis method to conclude which generator is preferable for our further investigation.

3.2.1 Decay of Singular Values

The first step is to investigate the decay of the singular values computed by `analysisSVD.m` in Matlab. Recall, we want the singular values of the transformation matrices to decay as the ones from $\mathcal{R}(\Omega)$. Additionally, we note that

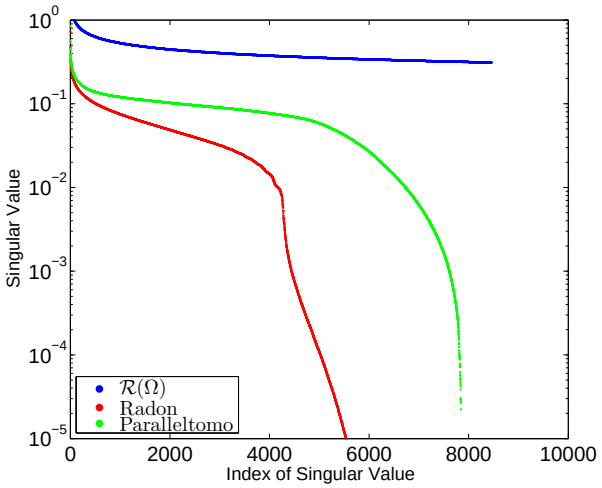

Figure 3.4: Singular values $\mathcal{R}(\Omega)$, the transformation matrix from Matlab's `radon.m` and the transformation matrix from `paralleltomo.m` (of the same size).

from now on, when comparing the decay of the singular values, we normalize them with respect to their largest values. In Figure 3.5 we observe that the decay of the singular values from `paralleltomo.m` and $\mathcal{R}(\Omega)$ are similar until around the 4000th singular value. However, the decay of `radon.m` is much steeper in the beginning which could indicate that it does not mimic the analytic Radon transformation that well. For this example it looks like `paralleltomo.m`'s transformation matrix gives a better approximation for $\mathcal{R}(\Omega)$, and the same behaviour is present for different sizes of A.

Remark. The steep decay of the singular values for `radon.m` might be explained by how it gathers the projection data. Unlike `paralleltomo.m` the method takes the average of four *sub-projections* when creating a normal projection, as described in the documentation of `radon.m`. This method of gathering projections might better simulate real CT measurements, but it is out of the scope of this thesis to investigate this proposition.

Indeed the decay of the singular values gives us an idea of how well we can expect a reconstruction to be. As expected, the singular values for the discretised problem decay much faster than the analytical one. The important insight is gained by considering the rate of decay. A slower decay means more information of the object can be reconstructed, since the range of the transformation matrix will increase, as explained in Remark 2.9. In this case, we could then expect

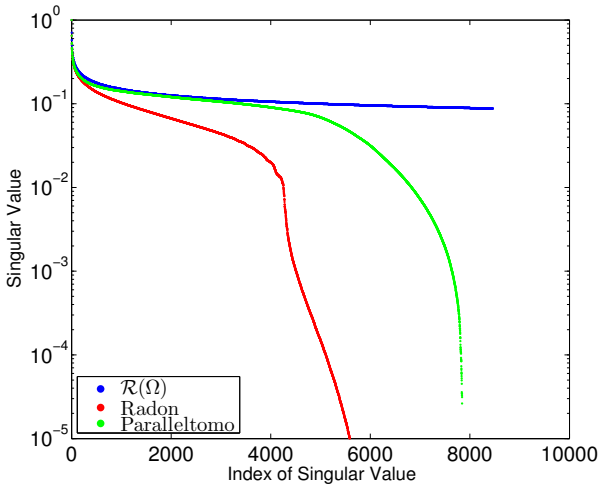

Figure 3.5: Decay of singular values for `radon.m`, `paralletomo.m` and $\mathcal{R}(\Omega)$.

that reconstructions of `paralleltomo` projections to be better than projections obtained from `radon.m`. Continuing with the analysis, we will see further justification of this statement.

3.2.2 Discrete Picard Condition

We recall that if the DPC is not satisfied the norm of the solution will become too large in practice. Thus, we only want to include the singular values, σ_i, and left singular vectors, $\mathbf{u}_i$, that satisfy the DPC when considering practical problems. To begin with, we note that the DPC will be stricter than just choosing all singular values below the rank of the transformation matrix, A. This is due to the fact that the DPC includes information about the measurements, $\mathbf{b}$, which for this case have an added relative noise level of $\eta = 5\%$. In this step, we will then investigate how the index, i, satisfying the DPC, compare for the two transformation matrices. To clarify this: The one with the highest index will likely have a better reconstruction when the system contains noisy measurements. Recall that the DPC (Theorem 2.11) is satisfied when the coefficients $|\mathbf{u}_i^T b|$ (red) decay faster than the corresponding singular values (blue) on average. The ratio of the decay is shown as the black dots in the plots, and we denote these as the Picard values. In Figure 3.6 we see that the first time the DPC is not satisfied for `radon.m` is around the 3000th singular value. For `paralleltomo.m` we find this index to be around the 5000th singular value. Thus, only considering this,

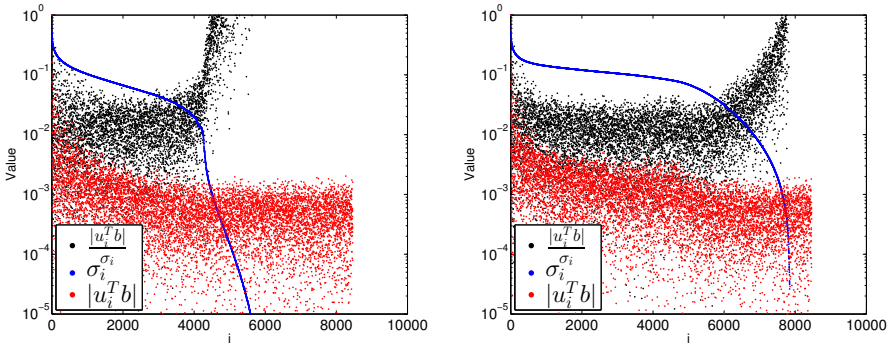

(a) `radon.m` (b) `paralleltomo.m`

Figure 3.6: Picard plot for `radon.m` and `paralleltomo.m` with relative noise level $\eta = 5\%$. The Picard values (black), singular values (blue) and coefficients $|\mathbf{u}_i^T\mathbf{b}|$ (red) of the DPC are shown together.

we can conclude that matrices generated from `paralleltomo.m` should be able to get better reconstructions for systems with noisy measurements. We do note, however, this is only true when both systems model the method of generating the measurements equally well. As we mentioned, `radon.m` might model the physics of a CT scanner better. But since the purpose of this thesis is to study how changes in structural parameters, such as angular range and domain size, influence reconstructions, we prefer a simple mathematical model.

3.2.3 Structure of Singular Vectors

The third step is to investigate the right singular vectors $\mathbf{v}_i$. These form a basis for the space containing the object $\mathbf{x}$. By investigating the basis, we are able to predict what kind of structure we can expect the reconstructing to contain. `AnalysisSVD.m` gives us the first 12 singular vectors and the first six not satisfying the DPC. It finds the index for when the DPC is not satisfied by simple linear regression. The method keeps including singular vectors up until the linear fit of the Picard values is an increasing function. This is a simple approximation to how one would visually determine the index for which the DPC is not longer satisfied.

In Figure 3.7 we have the singular vectors from the two different transformation matrices. The colour scheme we apply is the standard one used by Matlab, where shades of blue represents low values and shades of red are high. The

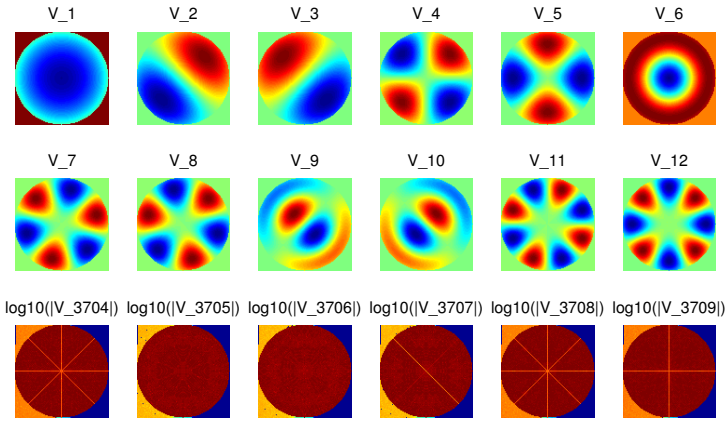

(a) Singular vectors from `radon.m`

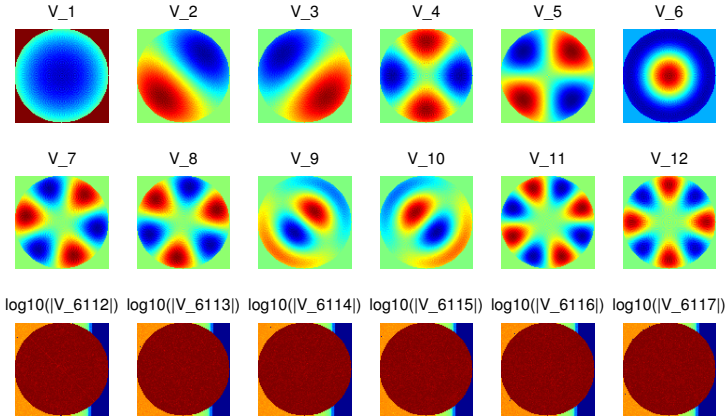

(b) Singular vectors from `paralleltomo.m`

Figure 3.7: The first 12 singular vectors and the first 6 not to satisfy the DPC.

colour indexing is done individually for each singular vector to highlight as much structure as possible. The first thing to notice is that we have a lot of different basis vectors available for the reconstruction. Even with a linear combination of a small amount of singular vectors we can expect to reconstruct fairly complex structures. As expected the singular vectors increase in frequency in all directions along with the index number. The last six singular vectors look very high frequent, hence they are not useful basis functions for the overall structure of the object. From our theory we know that these high frequency components will be dominated by noise in the inverse problem and thus we can expect some details to disappear from reconstructions, while the overall structure should be intact.

3.2.4 Reconstructions

Since we have the true object $\mathbf{x}^{\text{exact}}$, we are with the theory from Equation 2.9 able to determine the elements of $\mathbf{x}^{\text{exact}}$ that are in the range and the null space of the transformation matrix, A. Figure 3.8 shows that the range of A contains nearly all of $\mathbf{x}^{\text{exact}}$ and hence it should be possible to make a proper reconstruction of the image, which is just as we expected from the earlier steps in our analysis.

`analysisSVD.m` ends with trying two different reconstruction methods on the problems. Figure 3.9 shows that the reconstructions from the Landweber method are more or less alike and as we expected, the reconstructions contain the overall structure of the object, however, some details are missing. The reconstruction from `paralleltomo.m` contains more of these details: We are able to observe the small light dots in the bottom of the outer circle. The reconstructions from the truncated singular value decomposition are very similar, and we can not favour one transformation matrix over the other by the naked eye. To probe further, we can calculate the relative error ε by

$$\varepsilon = \frac{\|\mathbf{x}^{\text{exact}} - \mathbf{x}\|}{\|\mathbf{x}^{\text{exact}}\|} \tag{3.1}$$

`analysisSVD.m` outputs this in the command window when running the analysis. We find the relative errors as follows:

```
Radon: TSVD relative error = 0.419465
Paralleltomo: TSVD relative error = 0.361925
Radon: Landweber relative error = 0.286777
Paralleltomo: Landweber relative error = 0.219639
```

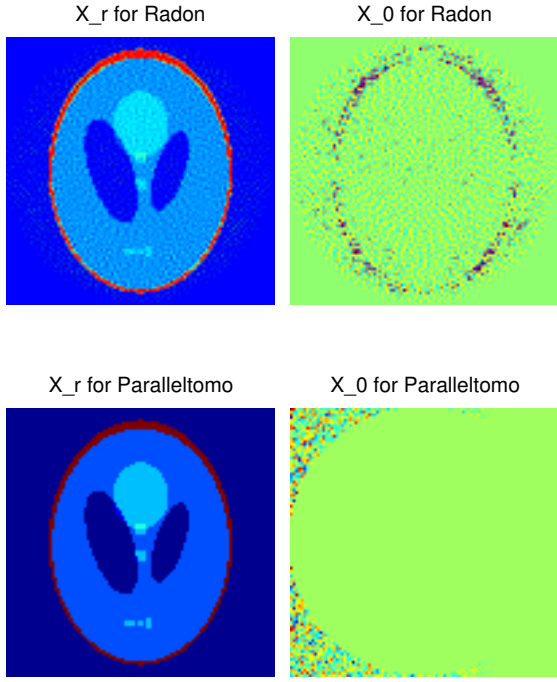

(a) Range **(b)** Null space

Figure 3.8: Elements of $\mathbf{x}$ in the range and null space of A.

So by this estimate of the error, we can conclude that the reconstructions from `paralleltomo.m` are slightly better ($\approx 6\%$).

3.2.5 Summary

We have now used the analysis method to motivate the choice of a transformation matrix that, in terms of its SVD, is similar to our mathematical model for X-ray tomography, the Radon Transform. We saw, surprisingly, that the `paralleltomo.m` method was more similar, in term of its singular values, to the analytical Radon transform than Matlabs own `Radon.m`. We argued this could be due to how `Radon.m` gathers the projection data. The final conclusion was, that since `paralleltomo.m` also performed better for the simulated test problems with the standard TSVD and Landweber reconstruction methods, it was chosen as transformation matrix generator for the rest of the thesis.

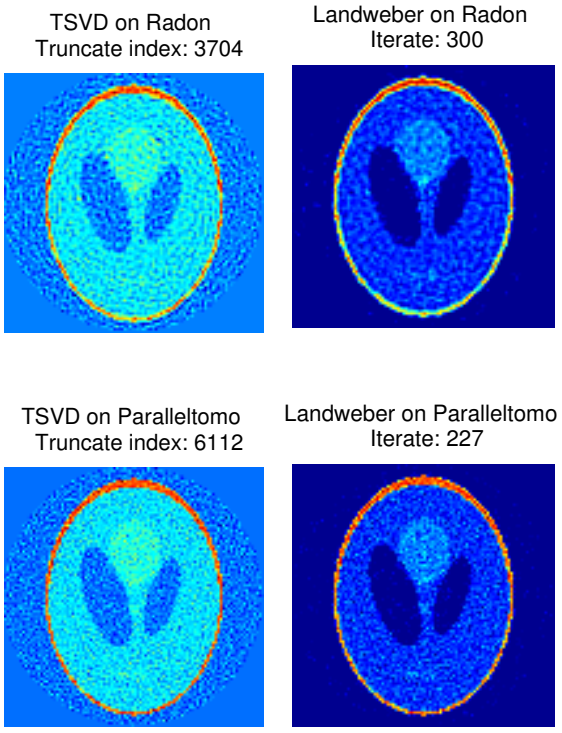

Figure 3.9: Reconstructions using the TSVD and Landweber methods.

3.3 Tomography on Different Domains

So far, we have considered objects on circular domains, since our theory is built on this basis. However, in real life problems, this is not always the case; e.g. in the airport security system where hand luggage is scanned. Here suitcases, computers, ect. are scanned on a rectangular domain. Hence, we are motivated to investigate tomographic on various domains. Throughout this section, we will compare the tomographic systems for three different domains, namely

- Circular domain
- Square domain
- Rectangular domain

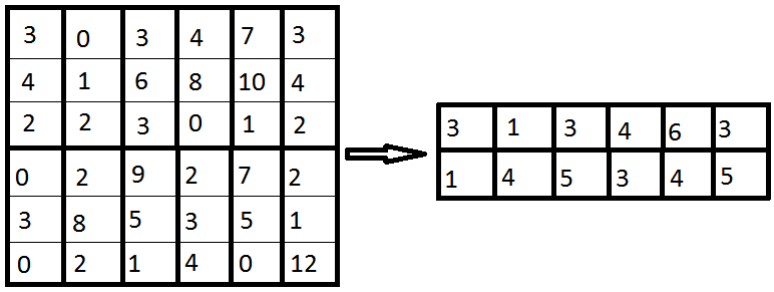

Figure 3.10: Changing a object from a square, $\mathbf{x}_s \in \mathbb{R}^{6\times 6}$, into a rectangle one, $\mathbf{x}_{re} \in \mathbb{R}^{2\times 6}$, for $\alpha = 2$.

In the previous section we decided to consider only the transformation matrix from `paralleltomo.m`, since we concluded that it was a better approximation to the analytic Radon transformation.

To test these set-ups, we need to create appropriate transformation matrices for the systems on the different domains. The transformation matrix from `paralleltomo.m` is square, we call this $A_s \in \mathbb{R}^{m\times N^2}$. For the circular domain we will use the mask as in the previous section but without changing to unit size. This transformation in domain is done by `changeDomains_circle.m`. Using the mask we "remove" pixels and hereby decrease the amount of useful data. To offset this decrease, we first find the ratio of the area between the square and circular domain as $\frac{N^2}{(N/2)^2\pi} = \frac{4}{\pi}$. To get the area of the circle $\frac{4}{\pi}$ times bigger, we need to multiply the diameter by $2/\sqrt{\pi}$. We therefore denote the transformation matrix of the circular domain as $A_c \in \mathbb{R}^{m\times(\lceil 2N/\sqrt{\pi}\rceil)^2}$.

Remark. To get rays through the corner pixels from all angles of a $N \times N$ square object, one have to use a detector of size $\sqrt{2}N$. But when working with a circular domain with diameter N, one does not have this issue and can preferably use a detector of size N. This is taking into consideration in `main.m` when calling `paralleltomo.m` for the circular domain.

To create a rectangular object for which we can simulate tomographic measurements, we will squeeze the square object by averaging sets of its rows. To do this, we divide each column into a certain number of blocks, α, with N/α elements in each block. We then squeeze each of these blocks into one pixel, such that the pixel value is the average of the block, as illustrated in Figure 3.10. By doing this, we have reduced the number of rows in the object by α, and thus to compensate for this reduction in pixels, we will have to use a α times bigger object initially. The rectangular object is then $N/\alpha \times N\alpha$ in size. We

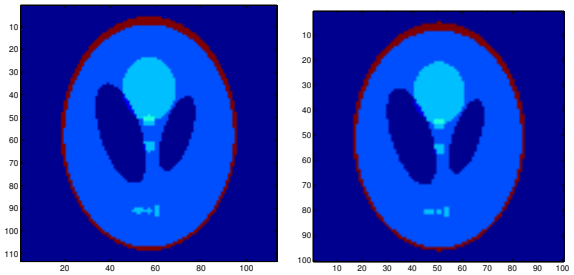

(a) Circular (b) Square

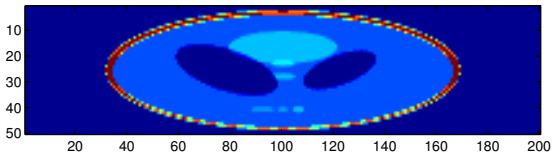

(c) Rectangular

Figure 3.11: The Shepp-Logan phantom in different domains for $N = 100$ and $\alpha = 2$.

denote the transformation matrix for the rectangular domain as $A_{re} \in \mathbb{R}^{m \times N^2}$. The rectangular object is created in `myphantom_rect.m` and the corresponding transformation matrix, A_{re} in the script `paralleltomo_rect.m`, which is a modification of `paralleltomo.m` that works with rectangular domains.

The three objects, all with about N^2 pixels inside the domain, are illustrated in Figure 3.11, where the number of rows and columns are shown. In this section we will for the square and rectangular domain use projection sets of size $\lceil \sqrt{2}N \rceil$ and a detector of size $d = \lceil \sqrt{2}N \rceil$. For the circular domain we will use the detector size $\lceil 2N/\sqrt{\pi} \rceil$, since this is the domain width from every angle. In all the examples we use an angular range of $[0, 179]$ with sets of projections sent from every third degree. Now we have the three set-ups namely

- $A_c \mathbf{x}_c = \mathbf{b}_c$, where $A_c \in \mathbb{R}^{m \times (2N/\sqrt{\pi})^2}$,$\mathbf{x}_c \in \mathbb{R}^{(2N/\sqrt{\pi})^2}$, $\mathbf{b}_c \in \mathbb{R}^m$
- $A_s \mathbf{x}_s = \mathbf{b}_s$, where $A_s \in \mathbb{R}^{m \times N^2}$, $\mathbf{x}_s \in \mathbb{R}^{N^2}$, $\mathbf{b}_s \in \mathbb{R}^m$
- $A_{re} \mathbf{x}_{re} = \mathbf{b}_{re}$, where $A_{re} \in \mathbb{R}^{m \times N^2}$, $\mathbf{x}_{re} \in \mathbb{R}^{N^2}$, $\mathbf{b}_{re} \in \mathbb{R}^m$

Remark. Even though $\mathbf{x}_c$ and the corresponding A_c is larger than the other objects and transformation matrices, it does not carry more information, since the excess number of elements are set to be zero.

3.3.1 Decay of Singular Values

This step is to analyse the decay of the singular values for the three different transformation matrices. In Figure 3.12, we observe that the singular values from the square domain has a characteristic decay: First a short steep decay, then a long gradual slope, and in the end a short steep one which phases out slowly until a sudden drop under 10^{-5}. Throughout the thesis, we consider all singular values under 10^{-5} too small to use in practise. The square domain follows the decay from the circular domain right up until the short steep decay at the end. The decay from the circular domain is the least steep of the three and have the most singular values above 10^{-5}. An explanation for this, could be that some rays in the square domain do not go through any pixels when the detector size is larger than one of the sides of the domain. This could lead to fewer linearly independent rows in the transformation matrix for the square and rectangular domain. When we look at the decay from the rectangular domain, we observe the same steep start as the two others. After the start it has a steady slope, just slightly steeper than the two others, and then it crosses the slope from the square at its final drop. The fact that the rectangular domain has more singular values above 10^{-5} compared to the square domain might indicate that it has fewer rays not going through any pixels in the domain. This makes sense since it only happens for projections sent from either the left or right side for the rectangular domain, whereas it happens for every side of the square domain.

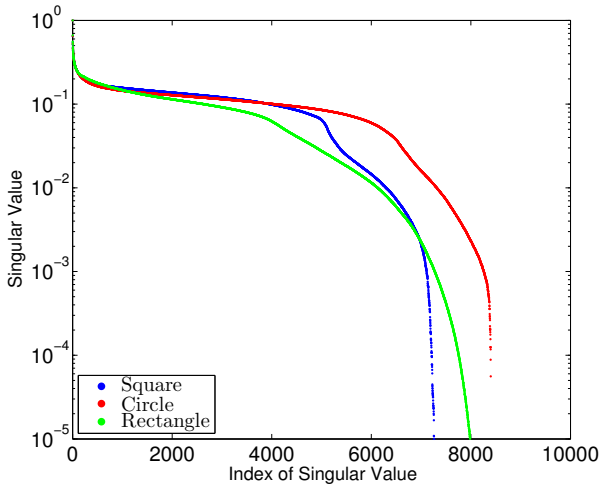

Figure 3.12: Decay of singular values for square, circular and rectangular domains

3.3.2 Discrete Picard Condition

In this step, we will check how many of the singular values, $\sigma_\mathbf{i}$ and their corresponding left singular vectors, $\mathbf{u}_i$ satisfy the DPC if the measurements $\mathbf{b}_s, \mathbf{b}_c$ and $\mathbf{b}_{re}$ has a relative noise level of $\eta = 0.5\%$.

Figure 3.13a shows the decay of the singular values, σ_i, the decay of $|\mathbf{u}_i^T\mathbf{b}|$ and the Picard values, $|\mathbf{u}_i^T\mathbf{b}|/\sigma_i$, for the square domain. Here we see that the DPC is satisfied up until around the 5000th singular value, when the singular values decay faster than the average of $|\mathbf{u}_i^T\mathbf{b}|$.

In Figure 3.13b, we observe for the circular domain that the DPC is satisfied up until the 6500th singular value. We can expect to use more high frequent singular vectors for the reconstruction and hence get more details. This might not be noticeable by the naked eye since it is very high frequent.

In Figure 3.13c, we observe that the DPC is met up until the 4000th singular value for the rectangular domain. The rectangular domain has the lowest index satisfying the DPC. Thus, for these systems with measurements containing a relative noise level of $\eta = 5\%$, we expect the best reconstruction from the circular and square domain. Here the reconstruction from circular domain will be slightly better than the one from the square. The worst reconstruction of the three would be from the rectangular domain.

3.3.3 Structure of Singular Vectors

The next step is to analyse the singular vectors of the three different domains. In Figure 3.14a, we have the singular vectors of the square transformation matrix, A_s. We observe a nice symmetry, and the structure is present all around the domain. If we look at the first singular vectors with index not satisfying the DPC, we realise that it is very high frequent and is not useful for the overall structure, only for small details. Since we know high frequency will be dominated by noise, it makes sense not to include these.

In Figure 3.14b we have the singular vectors of the transformation matrix on for the circular domain, A_c. These singular vectors carry the same nice structure as the ones from the square, and again the information seems to be distributed all around the domain. It is noticeable that the singular vectors obviously does not carry information outside the circular domain.

In Figure 3.14, we have the singular vectors of the transformation matrix from

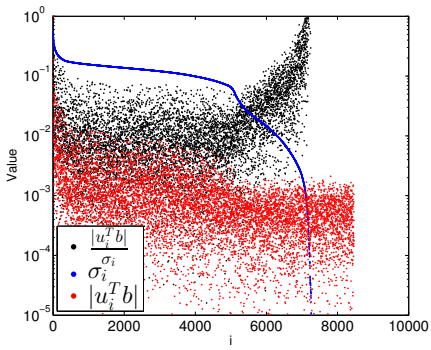

(a) Square domain

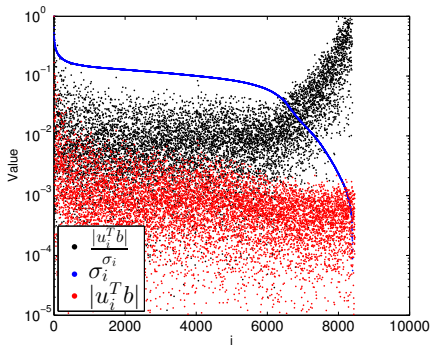

(b) Circular domain

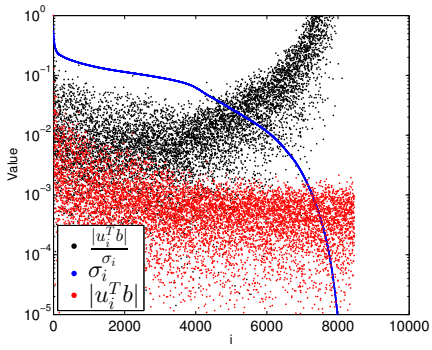

(c) Rectangular domain

Figure 3.13: Picard plot of different domains with relative noise level $\eta = 5\%$. The Picard values (black), singular values (blue) and coefficients $|\mathbf{u}_i^T \mathbf{b}|$ (red) of the DPC are shown together.

the rectangular domain, A_{re}. In general, it looks like there is a nice structure in the centre of the singular vectors. There is a lot of different formations in the middle. This is consistent with the fact that there is a higher density of rays going through the centre of the domain compared to the left and right side. The concern is the lack of structure outside the centre where the few elements all are close to horizontal in structure. The lack of elements in the sides of the basis vectors could make it difficult to reconstruct the corresponding sides of the object.

From this step we expect proper reconstructions of the objects in the square and circular domains. The reconstruction of the rectangular domain could lack structure in the left and right sides. This is likely caused by the lack of rays going through the right and left region of the object. We would like to investigate how many rays actually go through all regions of the rectangular domain. To do this we have created a spy matrix A_{spy}, such that $A_{\text{spy}}(i,j) = 1 \iff A_{\text{Re}}(i,j) \neq 0$ and otherwise zero. Then, if we sum every column of A_{spy}, we get a vector, $\mathbf{x}_{\text{spy}}$, with elements $\mathbf{x}_{\text{spy}}(i)$ consisting of the number of rays going through the ith pixel.

This $\mathbf{x}_{\text{spy}}$ is created in `main.m` and can be seen in Figure 3.15. Here we observe that the intensity of rays are much higher in the centre of the object than in the outer regions as we expected. This could be the cause of the lack of structure in the singular vectors for the rectangular domain.

3.3.4 Reconstructions

Since we have the privilege of knowing the true underlying objects $\mathbf{x}_s^{\text{exact}}$, $\mathbf{x}_c^{\text{exact}}$ and $\mathbf{x}_{re}^{\text{exact}}$, we are able to construct the elements of these objects that are in the range and null space of the transformation matrices A_s, A_c and A_{re} respectively. Figure 3.16 shows the elements of the objects in the null spaces of the transformation matrices. Here we are able to see what we cannot hope to reconstruct. Both in the square and the circular domain, we recognise our expectations, namely that there is not that much structure lost. It looks like the reconstructions will lose some intensity in the outer circle but otherwise the null space only contain high frequency structure. For the rectangular domain we see that the null space contain the left and right side of the outer circle, which we expected from the earlier steps.

Figure 3.17 shows the elements of the objects in the range of the different transformation matrices; in other words, the elements of the object we can hope to reconstruct. In the figure, we observe that the range from the circular domain is close to indistinguishable from the true object. The range from the square

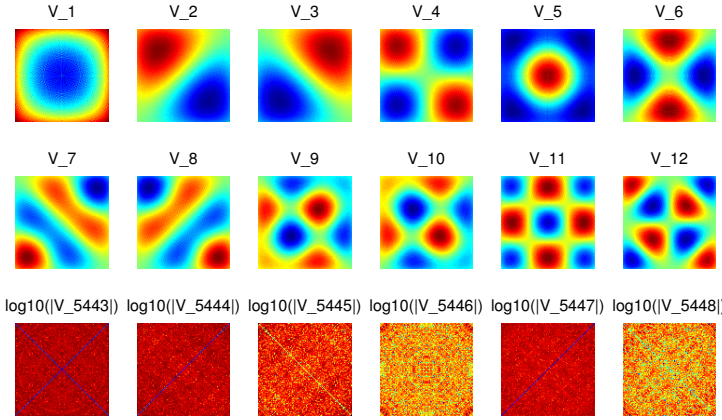

(a) Singular vectors from the transformation matrix for the square domain, A_s

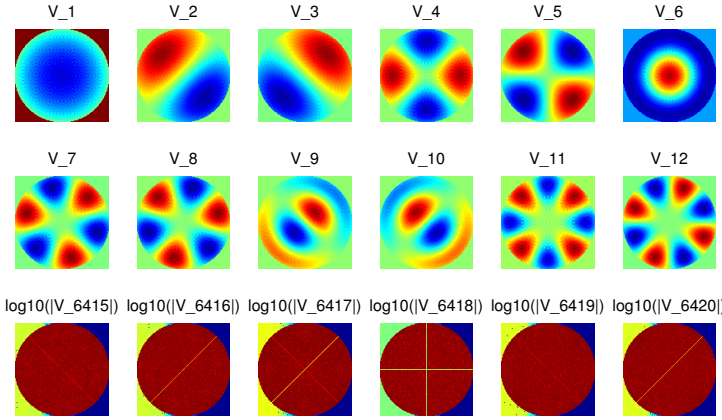

(b) Singular vectors from the transformation matrix for the circular domain, A_c

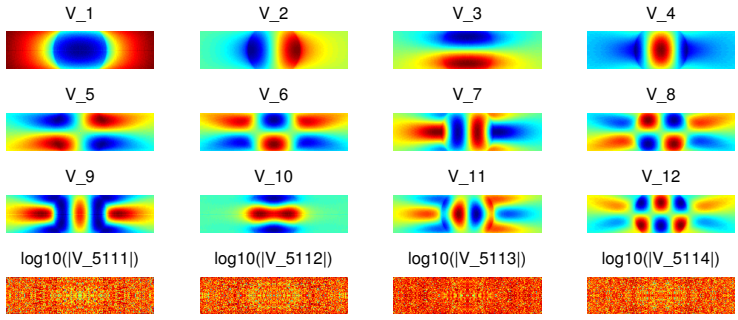

(c) Singular vectors from the transformation matrix for the rectangular domain, A_r

Figure 3.14: Right singular vectors, $\mathbf{v}_i$, for the different domains

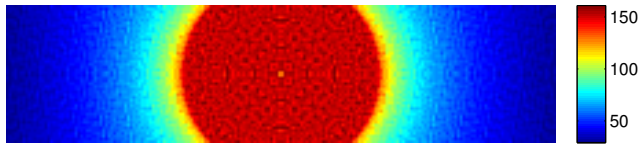

Figure 3.15: Illustration of how many rays are going through each pixel of the object.

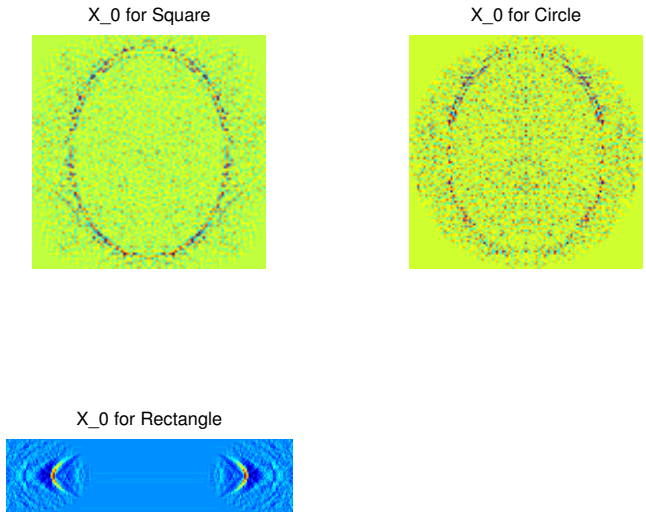

Figure 3.16: Elements of the objects in the null space of the different transformation matrices

domain does not contain all of the object but maintains the same structure. For the rectangular case we see that the range is missing the left and right outer ellipse, which we hence do not expect to be able to reconstruct.

In Figure 3.18, we observe that the reconstructions, for the circular and square domain, are equally good representations of the objects by the naked eye. However, for the rectangular domain, we observe the expected missing structure of the left and right side of the outer ellipse. Calculating the relative error by Equation 3.1, we find the following,

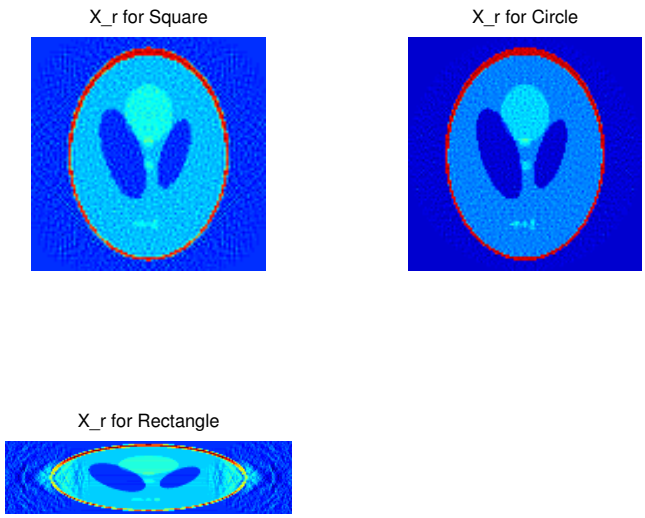

Figure 3.17: Elements of the objects in the range of the different transformation matrices

```
Square: TSVD relative error = 0.375218
Circle: TSVD relative error = 0.323993
Rectangle: TSVD relative error = 0.573137
Square: Landweber relative error = 0.225089
Circle: Landweber relative error = 0.229073
Rectangle: Landweber relative error = 0.441144
```

which confirms our visual observations.

3.3.5 Summary

In this section, we saw that if we used the fact that our object, the Shepp-Logan phantom, was circular, we could get better reconstructions than on a square domain with the same number of pixels. However, since the object one wishes to reconstruct is not always circular, and since the behaviour of the singular vectors on the square domain was similar to the circular one it is not a feasible general solution.

On the other hand, we saw that on the rectangular domain the reconstructions lose some information, even when taking projections all around the object on

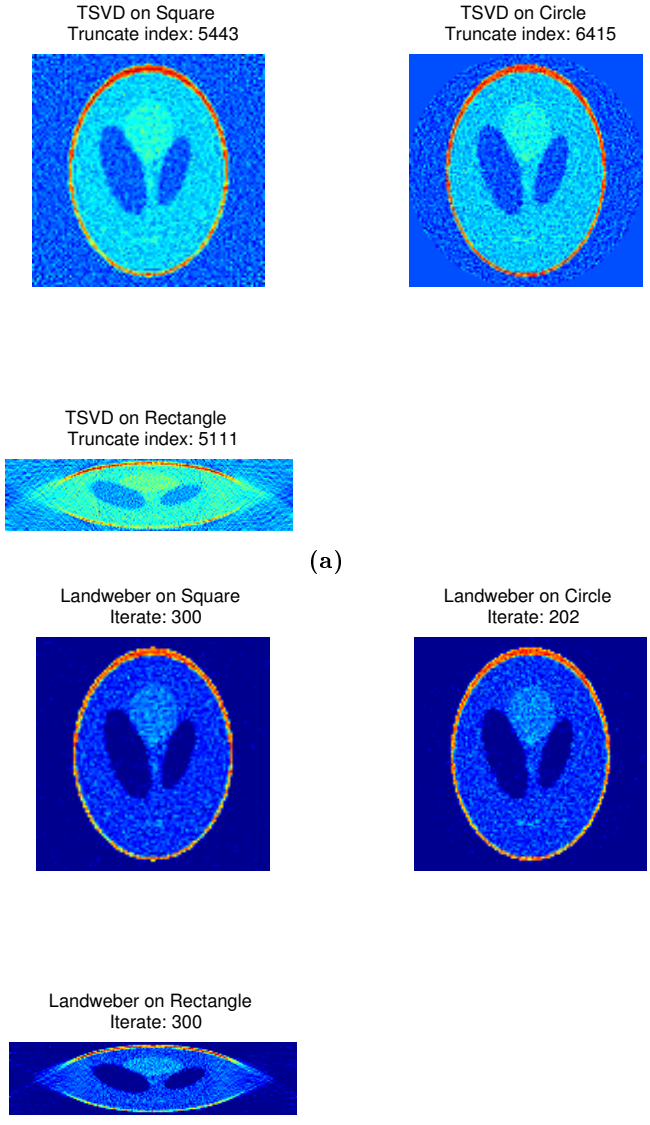

Figure 3.18: Reconstructions using the TSVD and Landweber methods.

equally distributed intervals. In particular, the left and right boundary of the Shepp-Logan phantom is stretched in the reconstructions. Interestingly when considering the elements of the object in the range of the transformation matrix for this domain, we see the left and right boundary is much more pronounced. Furthermore, we can see from the discrete Picard condition that the rectangular domain is more sensitive to noise.

3.4 Random Angle Tomography

As mentioned earlier an interesting area of tomography could be neutrino tomography, often used to detect the density distribution of the Earth [11]. However, in principle one could use neutrinos to image much smaller objects as well. We will not spend any time explaining how this process could work, except for the fact that the neutrinos will go through the object from random angles. This is due to the neutrinos arriving from radioactive decaying sources, such as suns and supernovae around the universe [12]. In this section, we will use our method of analysis to determine what effect projections arriving from random angles has on a tomographic problem compared to the normal structure we have seen throughout this thesis, namely that projections are equally distributed around the object.

To test this problem, we first have to find a way to simulate projections coming from random angles. An easy way to do this, and the one we have used in this section, is to create many projections from a large number of equally distributed angles and then pick out one at random. This projection would then be our projection from a random angle. This is done a sufficient number of times so that we has as many random angle projections as the total number of projections in the normal set-up. The code for this section is included in the `main.m` file. The file can be found here [9].

In this section, we work on a 100×100 domain with an object $\mathbf{x} \in \mathbb{R}^{N^2}$. We use $\lceil \sqrt{2}N \rceil$ projections with a detector of size $d = \lceil \sqrt{2}N \rceil$. *Normal* is denoted to mean the matrix with equally distributed angles that is normally used in our tomographic simulations. For the normal problem we send projections from angles $[0, 179]$ degrees equally distributed each third degree. This yields transformation matrices, for both the normal and random method, of size 8460×10000.

3.4.1 Decay of Singular Values

Again using `analysisSVD.m` based on our analysis method 3.1 we start out by considering the decay of the singular values. In Figure 3.19, we see the

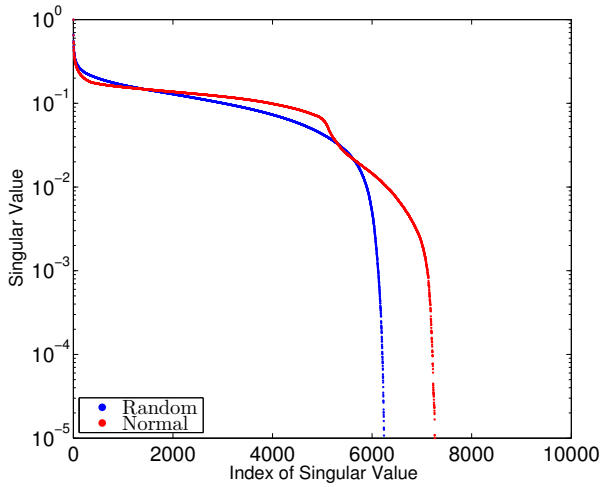

Figure 3.19: Decay of singular values for the normally structured problem and random angle problem.

decay of both the random and normal tomographic problem. Surprisingly, the singular values from the random angle matrix decay slower to start of with, but after the 2000th index it decays faster than the singular values for the normally structured matrix. However, on average the random angle singular values decay faster than the normal ones, and thus we can expect reconstructions from noise free measurements to be better for the normally structured problem.

Remark. It is worth noting that the singular values from the random angle problem decay more *smoothly*, than those of the normally structured problem. By smoothly we mean, that it does not have the long almost flat plateau we see from the 2000th to 5000th singular value for the normal matrix, and then a quick jump down around the 5500th singular value. Instead we see a smoother curve, although decaying faster on average.

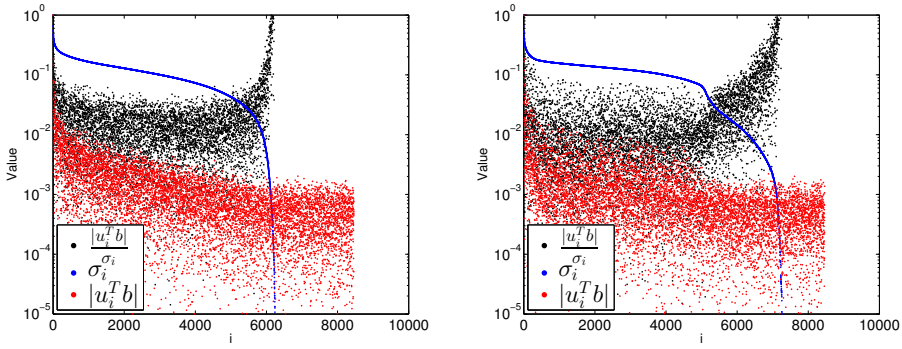

(a) Random angle problem **(b)** Equally distributed angle problem

Figure 3.20: Picard plot for the Random and normally structured problem with relative noise level $\eta = 5\%$. The Picard values (black), singular values (blue) and coefficients $|\mathbf{u}_i^T\mathbf{b}|$ (red) of the DPC are shown together.

3.4.2 Discrete Picard Condition

Before going through the results for the DPC, we remind the reader that there has been added a relative noise level of $\eta = 5\%$ to the measurements $\mathbf{b}$. This is the default noise level chosen by `analysisSVD.m`. In Figure 3.20, we see the Picard plots for both the random angle and equally distributed angle problems. For the random angle problem (Figure 3.20a), we see that the DPC is satisfied up until around the 4500th index. After this the singular values decay much faster than the corresponding coefficients $|u_i^T b|$. Likewise in Figure 3.20b, we see for the equally distributed angles that the DPC is satisfied up until around the 5000th index. Thus, we find no discernible difference in terms of the DPC alone for the two problems.

3.4.3 Structure of Singular Vectors

The next step in the analysis method is to consider the singular vectors. As shown in Figure 3.21a, we see the first 12 singular vectors of the random angle tomography problem, together with the first six singular vectors not satisfying the DPC. Interestingly, these are quite different from those of the normally structured transformation matrix as shown in Figure 3.21b. We notice the lack of smoothness on each singular vector. From this alone, we can expect, since the singular vectors are basis functions for the object $\mathbf{x}$, that reconstructions

from the random angles will appear less smooth and perhaps more jagged than reconstructions from the normally structured problem. On the same note, we see that the singular vectors that do not satisfy the DPC are very high frequent for both problems. We do note, however, a pattern in the singular vectors for the normally structured problem. When considering possible reconstructions in the next step of the analysis, we will look at the linear combination of these singular vectors to see if we can get any insight from this.

3.4.4 Reconstructions

Once again, since we know the true image, we can consider which elements of the object $\mathbf{x}^{\text{exact}}$ are in the range and null space of the transformation matrices. From Figure 3.22 we see that the null spaces for both problems look very similar. However, if we look at the range of the transformation matrix with random angles, we observe straight lines going through the domain. It is hard to speculate from where these artefacts originate, but we might see them in the reconstructions.

The reconstructions for the TSVD and Landweber methods are shown in Figures 3.23a and 3.23b respectively. We recognise the aforementioned lines on the reconstruction from the TSVD method, but on the one from the Landweber method they are gone. This suggests that the lines might be caused by the structure of the singular vectors since the TSVD method uses these for the reconstruction. However, further investigation into this particular subject has not been done. Instead, we consider only the difference in reconstructions from the Landweber method. We notice that, by the naked eye, there is no discernible difference between the two reconstructions. Calculating the relative error by Equation (3.1), we find:

```
Random: TSVD relative error = 0.476963
Normal: TSVD relative error = 0.370754
Random: Landweber relative error = 0.283099
Normal: Landweber relative error = 0.222167
```

We see that the normally structured problem have a lower relative error even for reconstruction from the Landweber method.

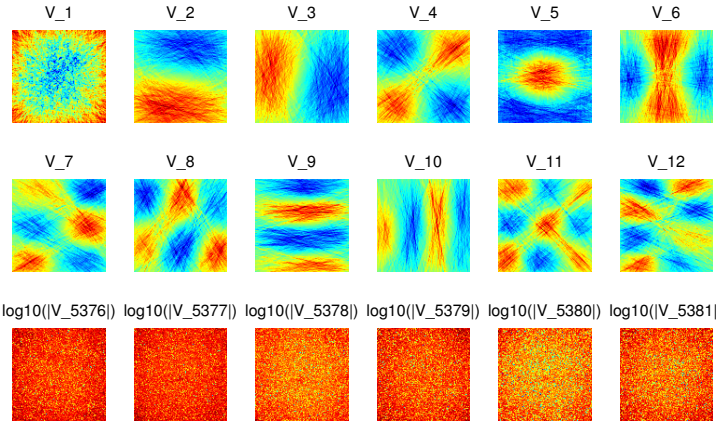

(a) Singular vectors of random angle transformation matrix

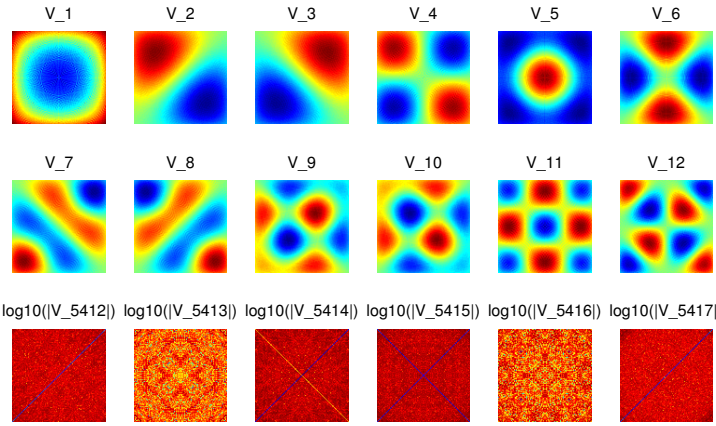

(b) Singular vectors of normally structured transformation matrix

Figure 3.21: The first 12 singular vectors and first six singular vectors not satisfying the DPC for the normally structured and random angle problems.

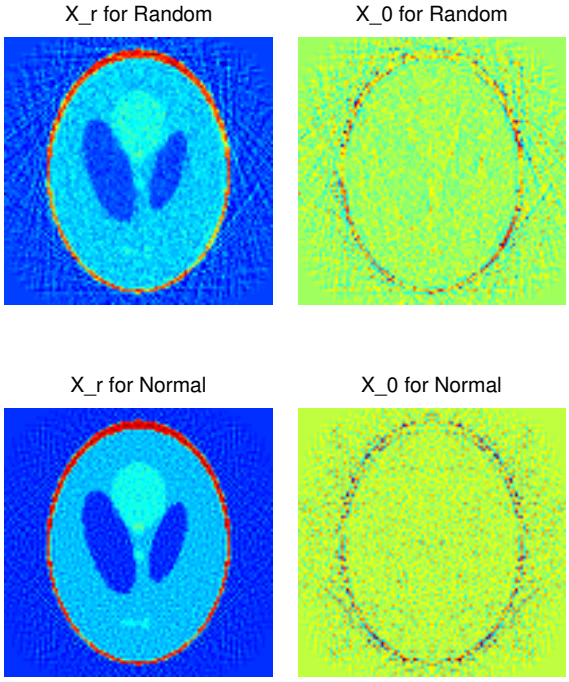

(a) Range **(b)** Null space

Figure 3.22: Elements of the object, $\mathbf{x}^{\text{exact}}$, in the range, X_r, and null space, X_0, of the transformation matrices.

3.4.5 Summary

In this section, we investigated the effects of randomly collecting projections rather than getting them in a structured manner. We saw that the singular vectors of the randomly collected projections were significantly different than those from the structured problem. However, when using the Landweber iterative method for reconstructions, we were only able to detect a small difference between the methods. We note that for sufficiently many projections there is no difference between collecting them randomly or equally distributed around an object.

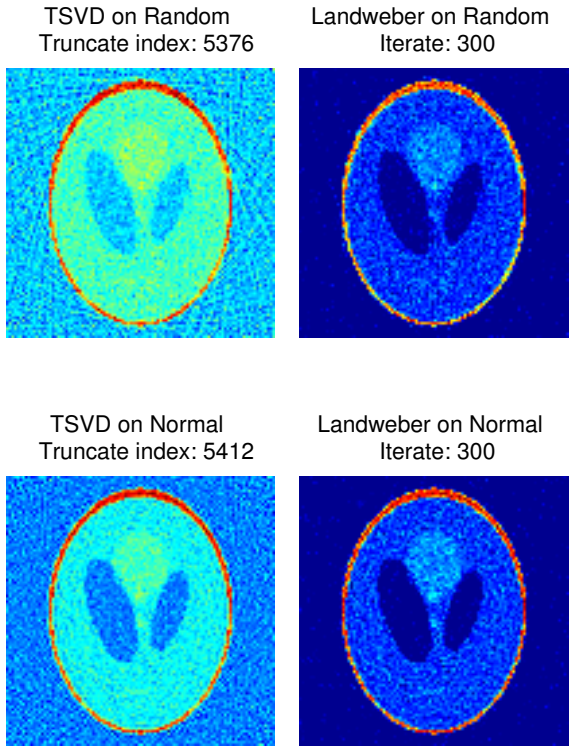

Figure 3.23: The reconstructions from the TSVD and Landweber methods for the normally structured and random angle problem.

3.5 Limited Angle Tomography

As we have learned throughout this thesis, it is not possible, in practise, to gather projection data from an infinite number of angles. We called the measurements gathered from a finite number of angles incomplete. However, in many practical applications, we run into another type of incomplete data, namely projection data from a limited angular range. In terms of CT, we call this *limited angle tomography*. For this type of tomography we have, in addition to the incompleteness of a finite number of angles, an incomplete angular range for the projection data. That is, projections may only be gathered from, say, 0 to 90 degrees, instead of from the whole 180 degrees of the half circle we have seen in earlier sections.

To test this, we have created six different transformation matrices. All act on a 100×100 domain, but each matrix has a different angular range. We denote A_ϕ to be the transformation matrix with angular range from 0 to ϕ degrees. The transformation matrices are created for the values of $\phi = \{179, 139, 99, 59, 39, 19\}$. To compare the methods in a meaningful way the number of projections collected per angle is kept the same, but the number of angles, in which we collect projections, is increased. This is done, such that, for smaller ϕ, there will be a smaller interval between the angles in which sets of projections are collected. The goal is to keep to total number of projections as close as possible so that each problem has the same amount of measurement data. Thus, all transformation matrices have ≈ 8460 rows and 10000 columns. The code for this section is included in the `main.m` file. The file can be found here in [9].

3.5.1 Decay of Singular Values

Like the previous set-ups, we can utilize `analysisSVD.m`. We start by considering the decay of the singular values. In Figure 3.24, we see the singular values of

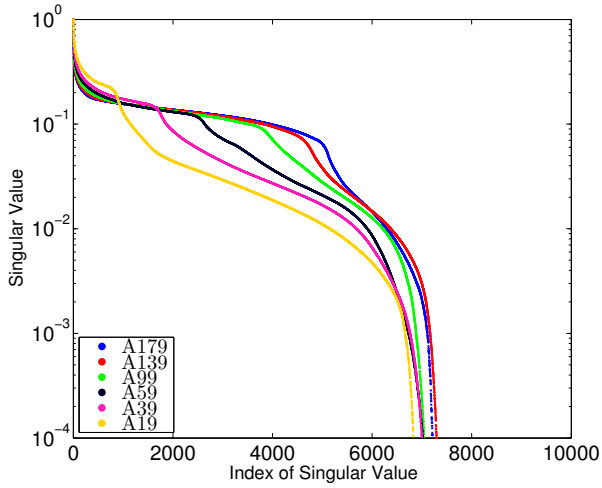

Figure 3.24: Decay of singular values for the six transformation matrices of different angular ranges.

all six angular ranges. Interestingly, when the angular range decreases so does the point at which the decay drops drastically to a steeper curve before decaying below 10^{-5}. Note that we have changed the limits of the axis in order to better show this difference in decay. It is clear that in this particular test problem, we

might be able to detect something about the angular range from the singular values of the corresponding transformation matrix. However, if we considered only the singular values, we would not expect reconstructions to be much different, since for all six transformation matrices the singular values decay below 10^{-5} at roughly the same index. In fact, if we were to do a TSVD reconstruction by truncating at the rank of the transformation matrix, we would expect this index to be very similar for all six problems. Unfortunately, as we have learned, truncating at the rank of the transformation matrix is not very useful when you have noisy measurement data. Thus we must consider the DPC.

Remark. We hypothesised that the point at which the decay of the singular values drastically drop, could be explained by the redundancy of the gathered projections. To test this, we limited the test problem to a smaller number of projections, say, only five from each angle, making the transformation matrix of size $\approx 300 \times 10000$ in the process. The result is shown in figure 3.25. Here we see that, even for a low total number of projections, the singular values still decay faster for the lower angular range problems. The singular values still have the same index when they hit the value 10^{-4}. Testing this for both lower (very under determined) and higher (very over determined) total number of projections gives the same results. Even changing the domain to a disc does not influence this behaviour. Thus, the faster decay of the singular values seem to be caused by gathering the projections from a limited angular range.

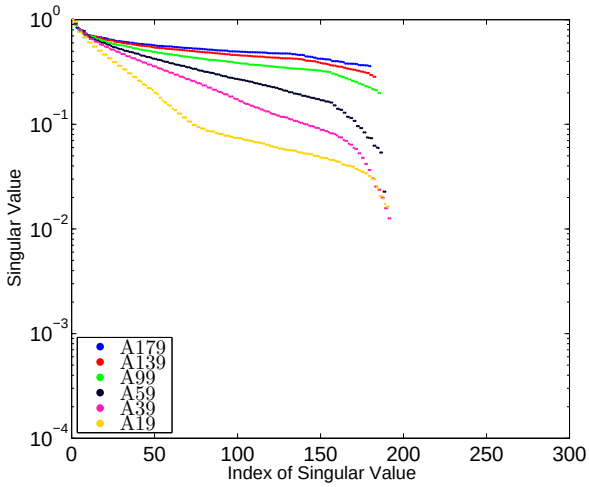

Figure 3.25: Decay of singular values for the six very under determined transformation matrices of different angular ranges.

3.5.2 Picard Condition

In Figure 3.26 we see the Picard plots for all six angular ranges. Again we recall that the DPC (Theorem 2.11) is satisfied when the coefficients $|\mathbf{u}_i^T\mathbf{b}|$ (red) decay faster than the corresponding singular values (blue) on average. The ratio, Picard values, of the decay is shown as the black dots in the plots.

For the full angular range problem, shown in Figure 3.26a, we see that the DPC is satisfied up until around the 5000th index. After this the singular values decay much faster than the corresponding coefficients, $|\mathbf{u}_i^T\mathbf{b}|$. For the angular ranges $[0, 139]$ and $[0, 99]$ degrees, we see, in Figure 3.26b and 3.26c, that the DPC is satisfied up until the 4500th index. However, after this we see the index decreases drastically to the 3000, 2000 and 1500 for the transformation matrices with angular ranges $[0, 59]$, $[0, 39]$ and $[0, 19]$ degrees, respectively, as shown in Figures 3.26d, 3.26e and 3.26f. Thus, when the measurement data is noisy, we can expect the reconstructions to be far worse for the problems with limited angular ranges.

3.5.3 Structure of Singular Vectors

The next step in the analysis method is to consider the singular vectors. Figure 3.27 shows the first 12 singular vectors of the different angular ranges, together with the first six singular vectors with index not satisfying the DPC. We have removed the subtitles of these plots to better utilize the space they take up. The bottom six singular vectors, $\mathbf{v}_i$, are still shown by plotting $\log_{10}(|\mathbf{v}_i|)$.

It is clear from the figure that, the structure of the singular vectors changes when we limit the angular range of the problem. The singular vectors become more and more vertical as the angular range decreases. Indeed, we could expect reconstructions for this particular choice of limited angles to be lacking any horizontal structure. For the Shepp-Logan phantom, we expect some of its boundary to vanish in reconstructions, due to the lack of circular structure singular vectors.

3.5.4 Reconstructions

Since we know the true image, we can consider what components of the object $\mathbf{x}^{\text{exact}}$ are in the range and null space of the transformation matrices. From Figure 3.28 we see that, as the angular range decreases, more and more elements

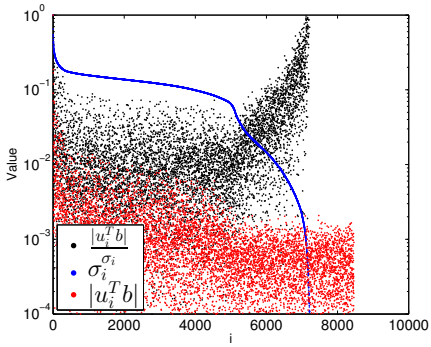

(a) Transformation matrix in angular range $[0, 179]$ degrees

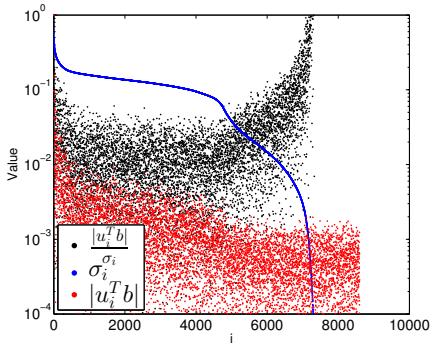

(b) Transformation matrix in angular range $[0, 139]$ degrees

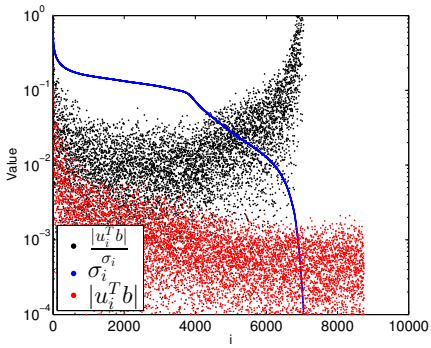

(c) Transformation matrix in angular range $[0, 99]$ degrees

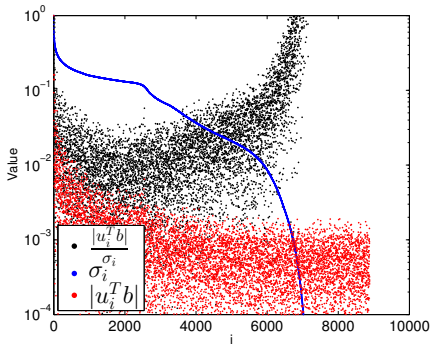

(d) Transformation matrix in angular range $[0, 59]$ degrees

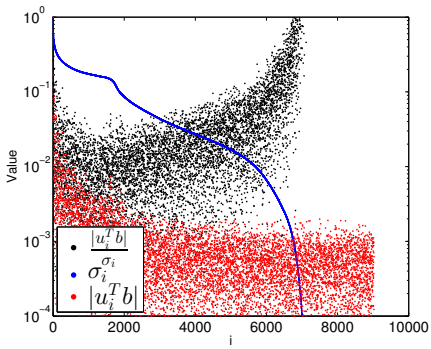

(e) Transformation matrix in angular range $[0, 39]$ degrees

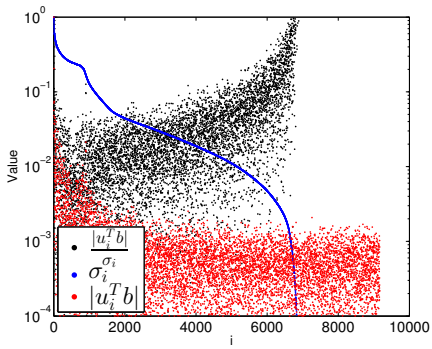

(f) Transformation matrix in angular range $[0, 19]$ degrees

Figure 3.26: Picard plot for the different angular range problems with relative noise level $\eta = 5\%$. The Picard values (black), singular values (blue) and coefficients $|\mathbf{u}_i^T\mathbf{b}|$ (red) of the DPC are shown together.

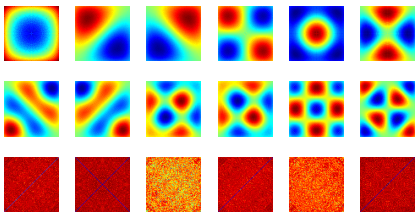

(a) Singular vectors from $[0, 179]$ degrees

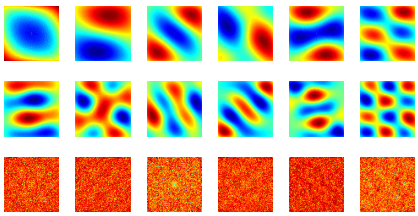

(b) Singular vectors from $[0, 139]$ degrees

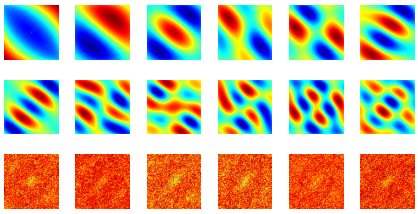

(c) Singular vectors from $[0, 99]$ degrees

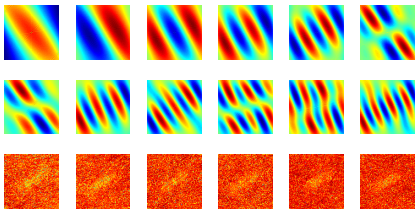

(d) Singular vectors from $[0, 59]$ degrees

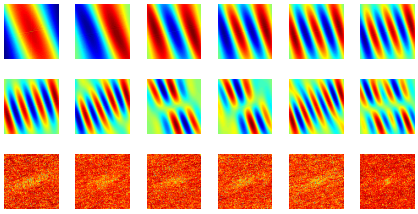

(e) Singular vectors from $[0, 39]$ degrees

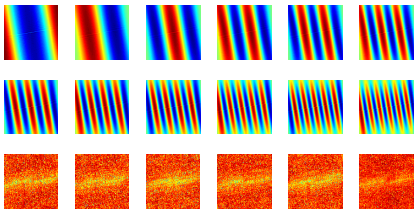

(f) Singular vectors from $[0, 19]$ degrees

Figure 3.27: The first 12 singular vectors and first six singular vectors with index not satisfying the DPC for all the six angular ranges.

go from being in the range to being in the null space of the transformation matrices.

When considering the reconstructions from the TSVD method, we recall that `analysisSVD.m` calculates the truncate index by linear regression with respect to the Picard values. Noting that the truncate index fits fairly well with our visual observations, we see exactly what we expected from considering the range of the transformation matrices. Both for the TSVD method, shown in Figure 3.29a, and Landweber method, shown in Figure 3.29b, the reconstructions lose more and more of their boundary when the angular range decreases. When the angular range is $[0, 19]$ degrees the reconstructions become almost unrecognisable.

3.5.5 Summary

In this section we saw that for problems with limited angular range the reconstructions become more susceptible to noise in measurements. However, for such problems there are still many elements in the range of the transformation matrix, which means that reconstructions from noise free measurements are much more similar. We noted that we seemed to be able to detect limited angular range by only considering the singular values or singular vectors.

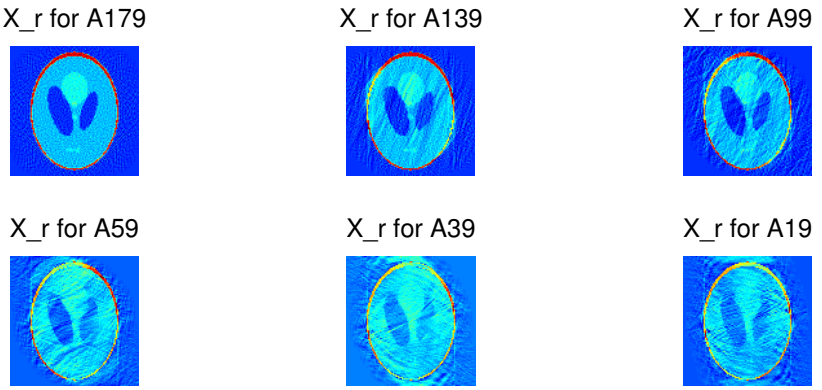

(a) Range

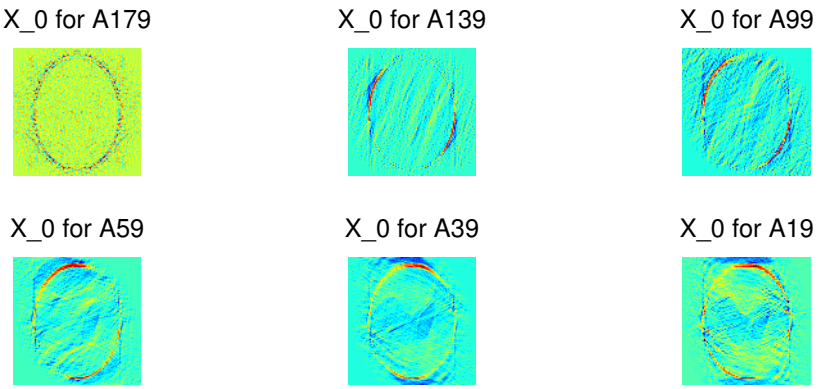

(b) Null space

Figure 3.28: Elements of the object, $\mathbf{x}^{\text{exact}}$, in the range, X_r, and null space, X_0, of the transformation matrices, A_ϕ

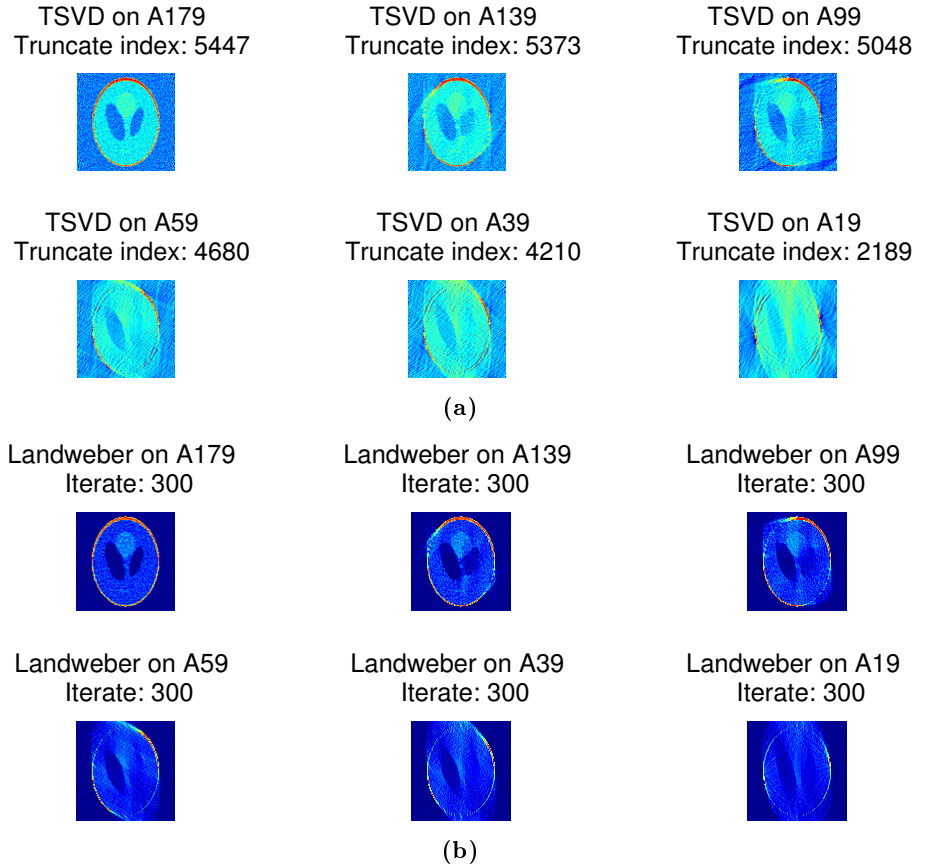

Figure 3.29: Reconstructions for all six angular ranges by the TSVD and Landweber method.

Chapter 4

Laminar Tomography

In this chapter we will investigate a type of tomography problems called *laminar tomography*. Laminar tomography is when we collect projections from a limited angular range as we saw in Section 3.5 and work on a rectangular domain as we saw in Section 3.3. Such problems arise naturally in practical applications like mammography, dental tomography, electron microscopy and in previously mentioned industry scenarios. In these types of problems, we will encounter most of the difficulties from the last chapter in one single problem.

We will use our analysis method to investigate the solvability of these problems. In this thesis we consider two laminar tomography problems. The goal of our analysis is to understand the inherent difficulties of general laminar tomography problems, where the purpose of these problems is to find anomalies in an otherwise homogeneous object.

We look at problems with a rectangular domain of size $N/\alpha \times N\alpha$. We will investigate an object with a repeating structural background and an alien structure inside the object. This alien structure is what we in this section will be searching for and trying to reconstruct. We will look at two different scenarios:

- In the first scenario the goal is to reconstruct an object with an alien structure of size $N/\alpha \times N/\alpha$, in the centre of the rectangular object, as shown in Figure 4.1.

- In the second scenario the goal is to reconstruct an object with an alien structure of size $\kappa \times \kappa$ for $\kappa < N/\alpha$, placed a distance, h, to the right of the centre as shown in Figure 4.2.

The background used in this section is created in `binarytomo.m` from AirTools [10]. This illustrates some horizontal structure which we know, from Section 3.5, is difficult to reconstruct with a limited angular range. We use the Shepp-Logan phantom as the alien structure. For our problem we have $N = 100$, $\alpha = 5$, $h = 50$ and $\kappa = 30$ which gives alien structures of sizes 50×50 and 30×30 for the two scenarios. The rectangular object is of size 200×50. The

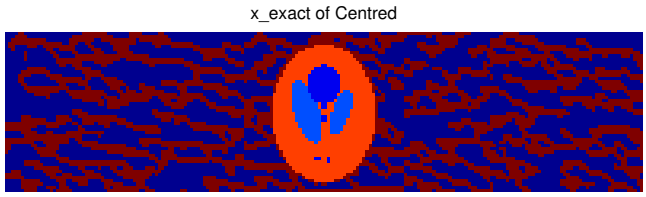

Figure 4.1: Laminar object with centred alien structure

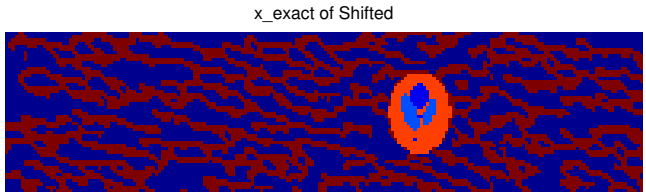

Figure 4.2: Laminar object with shifted smaller alien structure

transformation matrix for the systems is created by the previously mentioned function `paralleltomo_rect.m`, where we use $\sqrt{2}N/\alpha$ projections with detector size $d = \sqrt{2}N/\alpha$. The angular range is $[-50, 50]$ with sets of projections sent from every fifth degree, giving us a total number of projections $m = 1491$, so that we have the transformation matrix $A_L \in \mathbb{R}^{1491\times 10000}$.

Remark. Note that the two scenarios have the same transformation matrix, since they are on the same domain with the same sets of projections. Hence, step 1 and 3 of our method coincide for the two scenarios.

4.1 Decay of Singular Values

Again the first step is to study the decay of the singular values. This analysis will differ from the previous ones since we do not compare two transformation matrices but rather analyse one. In Figure 4.3, we observe the same structure of decay as the one from the square domain in Section 3.2. We observe that, in the laminar problem, the drop below 10^{-5} appears around the 1500th index of the singular values. This means that nearly all projections are linearly independent since $\text{Rank}(A) \leq \min(n, m) = m = 1491$. This makes sense since almost all projections go through some pixels that no other projection does. It is a bit misleading that the transformation matrix has such a high rank. This is because some pixels are represented only in one projection, and hence the rows in the transformation matrix are linearly independent.

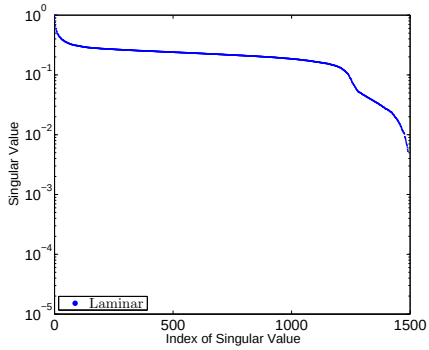

Figure 4.3: The decay of singular values for the laminar tomography problem

4.2 Discrete Picard Condition

The second step is to check for which index the singular values and vectors from the transformation matrix ceases to satisfy the DPC for both problems. Figure 4.4 shows us the decay of the coefficients, $|\mathbf{u}_i^T \mathbf{b}|$, the singular values, σ_i and the Picard values. We see that both scenarios are satisfying the DPC until around the 1200th index. For our TSVD reconstruction we then have 1200 right singular vectors to use as a basis. We notice that even with noise we can include almost all singular vectors up until around the rank of the transformation matrix. It seems like, for this small amount of projections, the systems might not be affected much by noise, even though they have a limited angular range.

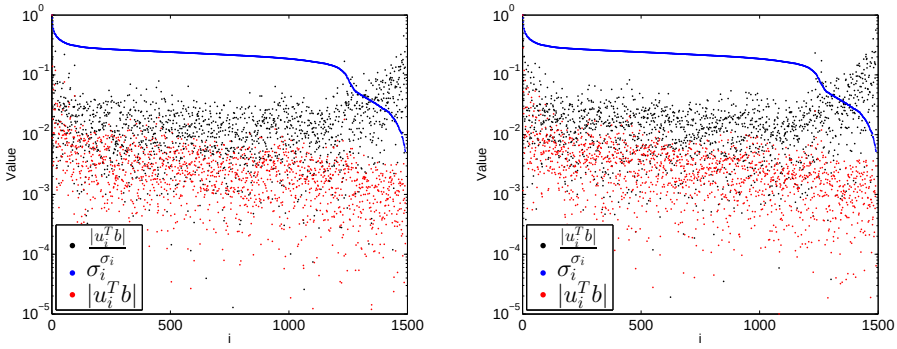

(a) Centred alien structure

(b) Shifted alien structure

Figure 4.4: Picard plots of the Laminar tomography problems with relative noise level $\eta = 5\%$. The Picard values (black), singular values (blue) and coefficients $|\mathbf{u}_i^T\mathbf{b}|$ (red) of the DPC are shown together.

4.3 Structure of Singular Vectors

Now that we know how many singular vectors we actually can use for the reconstruction, we will look at the structure of them. Recall that $\mathbf{v}_i$ are basis vectors for the domain containing the object. Figure 4.5 shows that our transformation matrix has a nice structure in the centre of its singular vectors. Since we do not have many rays going through the left and right area of the object, we see that we do not have any structure in the corresponding areas of the singular vectors. From this we expect the centre of the reconstruction to be much better than the left and right sides. We notice that this is the same behaviour as for the rectangular domain without limited angles. Since we in our second scenario have placed the alien structure $h = 50$ pixels from the centre, we expect it would be difficult to recognise it in our reconstruction.

Remark. In Section 3.3 we investigated the number of rays going through each pixel in the rectangular domain. We have done the same for our laminar problem. This gives us a vector, $\mathbf{x}_{\text{spy}}$, consisting of the number of rays going through each pixel in the domain. Figure 4.6 shows $\mathbf{x}_{\text{spy}}$. We observe, as expected, that the disc in the middle is the region with the highest density of rays. However, the number of rays in each pixel is significantly less than for the rectangular domain in Section 3.3. This might motivate us to use increase the number of projections, to see if we can provoke the behaviour, we saw for the limited angle problems in Section 3.5. This has been studied in Section 4.5.

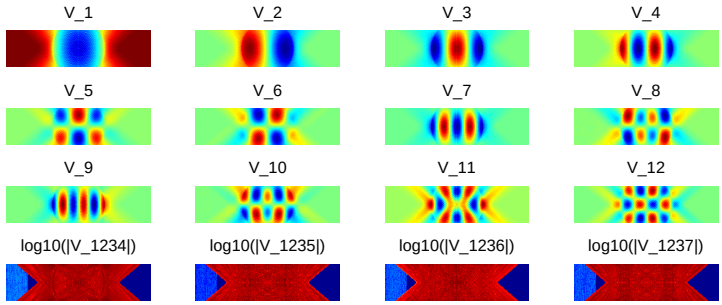

Figure 4.5: Singular vectors for the laminar tomography problem.

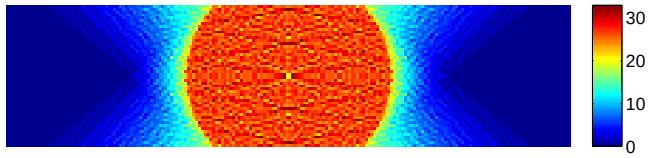

Figure 4.6: Number of rays going through each element of the domain

4.4 Reconstructions

Since we know the true objects, we are able to study which parts of them are in the range and null space of transformation matrix A_L. Figure 4.7a shows the elements of the objects in the range of A_L. For the first scenario, we are able to recognise some alien structure in the centre with the outline of the Shepp-Logan phantom. In the range of the second scenario we can locate the alien structure, but we are not able to determine any of its details. In Figure 4.7b, we see that the null space reflect these observations since most of the alien structure is in the null space.

We have reconstructed the two different scenarios, each by using both the TSVD and Landweber method. The reconstructions are shown in Figure 4.8. As we expected from studying the range of A_L, the reconstructions of the laminar problems do not contain the entire object. However, we are able to locate the alien structure for both scenarios using the Landweber method. They do not carry all of the details, but it is obvious where it is. For reconstructions using the TSVD method, especially for the second scenario, one has to know where to look, to find the alien structure.

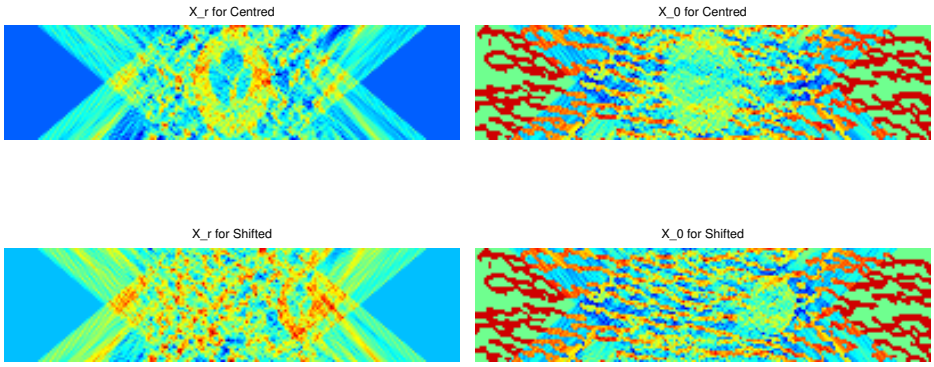

(a) The elements of the objects in the range of A_L

(b) The elements of the objects in the null space of A_L

Figure 4.7: The elements of the objects in the range and null space of A_L

4.5 Increased Number of Projections

From what we have learned in Section 4.3, we are motivated to repeat our laminar analysis with a larger total number of projections. We will not convey the full analysis but rather go through its key differences.

We increase the total number of projections by changing the interval of which we take sets of projections, similar to what we did in Section 3.4. We are now taking sets of projections at every degree, rather than every fifth. The transformation matrix is now of size 7171×10000. The rest of the parameters are left unchanged.

For the increased number of projections, we found the same behaviour for the singular values and vectors, and thus we felt no need to include these figures. Worthy of a note is that the decay of the singular values again dropped under 10^{-5} around the total number of projections, now 7171. The real difference occurs when we consider how the system is affected by noise.

In Figure 4.9, we observe that our range contains nearly all of the structure in the object. It actually seems possible to make a good reconstruction in our laminar tomography problem given sufficiently many **noise-free** projections. But as we have seen, the DPC tells a completely different story for noisy projections in limited angle problems. In Figure 4.10, we see the Picard plot for the problems. The index for which the DPC is no longer satisfied, around the 2000th index, is now much smaller than the rank of the transformation matrix. We note this

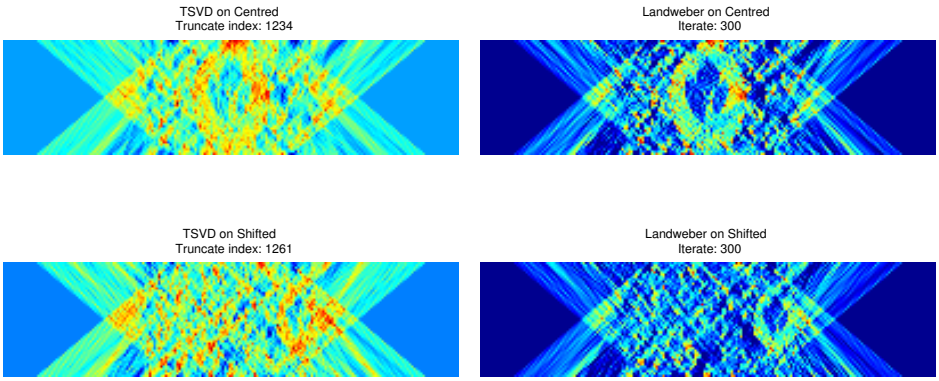

(a) TSVD method **(b)** Landweber method

Figure 4.8: Reconstructions made by the TSVD and Landweber method.

index is not much higher than for the previous problems with lower total number of projections.

In Figure 4.11, we observe that the reconstructions for both methods are very similar to the reconstructions for the problems with fewer projections. So it seems that laminar problems, as limited angle problems, are greatly affected by noise in measurements. Even increasing the number of projections do not increase the quality of the reconstructions by much.

4.6 Summary

From this chapter we learned from our SVD analysis that laminar tomography problems experience the same kind of difficulties as the limited angle and rectangular domain problems, we saw in Chapter 3. Indeed the lower the angular range is, the more the problem is dominated by noise in measurements. Additionally, we saw that, due to the low density of projections outside the centre of the domain, we cannot expect good reconstructions outside the centre.

We could not find additional characteristics, specific only to laminar tomography, since the results of the analysis was dominated by the aforementioned difficulties.

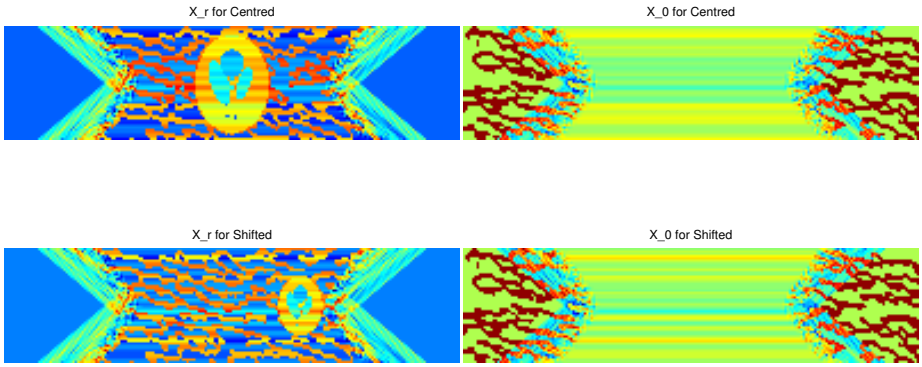

(a) The elements of the objects in the range of A_L using more projections

(b) The elements of the objects in the null space of A_L using more projections

Figure 4.9: The elements of the objects in the range and null space of A_L using more projections

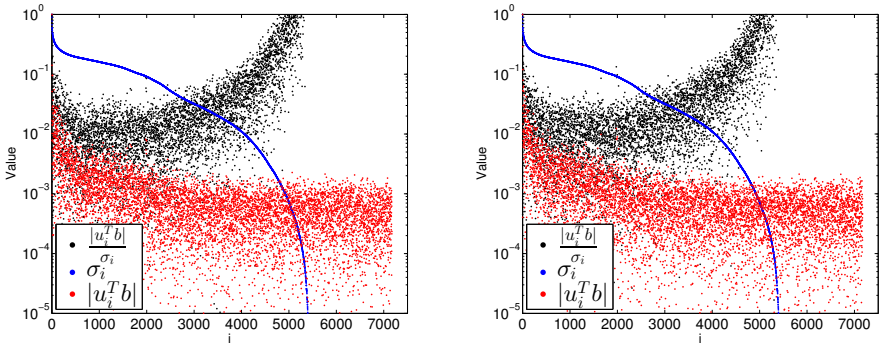

(a) Centred alien structure

(b) Shifted alien structure

Figure 4.10: Picard plots of the Laminar tomography problems with increased total number of projections and relative noise level $\eta = 5\%$. The Picard values (black), singular values (blue) and coefficients $|\mathbf{u}_i^T\mathbf{b}|$ (red) of the DPC are shown together.

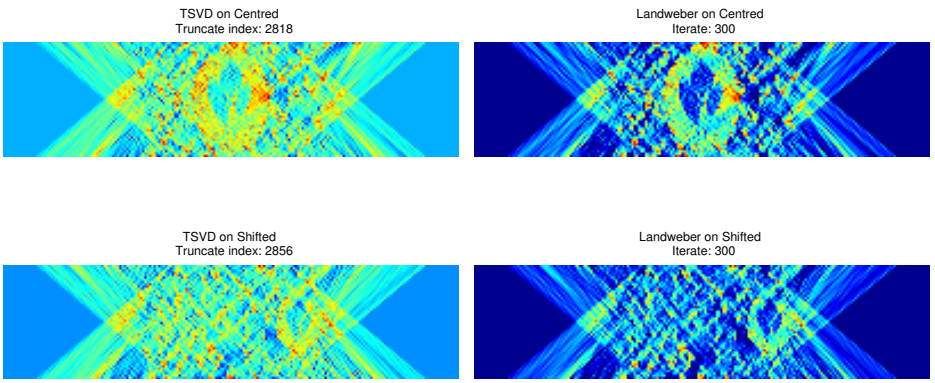

(a) TSVD method **(b)** Landweber method

Figure 4.11: Reconstructions of the laminar tomography problem with more projections

Chapter 5

Conclusion

In this thesis the goal was to study the solvability of specific X-ray tomography problems. Chapter 2 of the thesis laid the groundwork for how the analysis would be performed. The first part of the chapter considered these problems on continuous domains. Here we showed that small high frequent perturbations (read: noise), in the gathered measurements could dominate calculated solutions to the inverse problem, making it an ill-posed problem. By introducing the Picard condition, we showed that we could determine whether a specific problem would show this behaviour.

In the next part of the chapter it was shown that the ill-posed properties of the continuous domains could be carried over to the discretised versions of the problem. Here we showed that the discrete Picard condition could determine, not only if the problem would be dominated by noise, but also which specific components of the transformation would be dominated by the noise in the measurements, $\mathbf{b}$. This then gave us the desired tools to analyse the solvability of CT set-ups as described in Section 3.1. The results obtained from this method of analysis, on several problems, is listed below.

In Section 3.2, we concluded that the transformation matrix generated from `paralleltomo.m` – found in AIR Tools [10] – was a better approximation to the analytical Radon transform than the transformation matrix generated, from Matlab's own `Radon.m` function in terms of its SVD. Thus, it was used for the

remainder of the thesis to generate test problems that were more consistent with the theory from Chapter 2.

In Section 3.3, we concluded that the shape of the discretised domain could have an impact on the SVD and quality of reconstructions. More specifically, we saw that in a rectangular domain the area, in which we can expect good reconstructions, is limited by the total number of projections and how we send them through the object. For equally distributed angles all around the domain, with a detector of the mean of sizes of the domain sides, and a total number of projections, such that the transformation matrix of the system was slightly under determined, we saw that the quality of the reconstruction was only good in the centre of the domain.

In Section 3.4, we concluded that measurements gathered from random angles, in the contest of this thesis, had a negative impact on the quality of the TSVD reconstructions. However, we saw that for sufficiently many measurements the order and direction of the measurements was insignificant as long as they had the possibility of entering all around the object. We concluded that for problems where the number of projections is large enough, such that the transformation matrix is only slightly under determined, the difference in quality of reconstruction was negligible when using iterative reconstruction techniques, such as the Landweber method.

In Section 3.5, we concluded that limiting the angular range of measurements, severely impacted the quality of reconstructions when there was noise in the measurements. We also saw that without noise, the impact of limiting the angular range was less pronounced. We noted that it looked like the impact of limiting the angular range was independent of the total number of measurements done used in the problem.

Chapter 4 of the thesis consisted of applying the method of analysis and results from Chapter 3 to analyse laminar tomography problems. In the Sections 4.1-4.4, we concluded that the problem of laminar tomography exhibited the same properties noted for general rectangular domains. However, the impact of noise in measurements to the quality of reconstructions was not clear. Only in Section 4.5, could we conclude that, given enough projections, the laminar tomography problems also exhibited the properties of limited angle problems. Thus we concluded that reconstructions from laminar tomography problems, with sufficiently many projections, can be severely impacted by noise in measurements on top of the difficulties noted for rectangular domains.

All in all we have seen that an SVD based analysis can give valuable insight into the difficulties of complex tomography problems, such as that of laminar tomography.

5.1 Future Work

Here we list the areas of the thesis that we, due to the time limitation of a 15 ECTS B.Sc thesis, did not consider in detail even though they were of interest in relation to the subject of the thesis.

In Section 2.7, we argued that the Radon transform would have the same ill-posed properties as the deconvolution problem. The explanation, given in this thesis, was an intuitive way of comparing the two integral equations. In a future project, it could be beneficial to perform a rigorous comparison such that one might precisely define how the ill-posed properties carry over from the deconvolution problem to the Radon transform.

In Section 3.2, we saw that the transformation matrix generated from `radon.m` had singular values which decayed much faster than those of the analytical Radon transform. We argued that this could be due to how the method gathered its projections, namely by averaging over four sub-projections. In a future projection it could be interesting to see whether this method of gathering projections better model the physics of a CT-scanner, compared to the approach of modelling X-rays by a single line in the analytical Radon transform.

In Chapter 4, we studied two specific laminar tomography problems and concluded, from our method of analysis, that they exhibit some of the same characteristics as we saw in rectangular domains and limited angle problems. Another interesting method of analysis could be microlocal analysis, which is used to detect singularities in the sinogram for an X-ray tomography problem. In a future project it could be interesting to study how microlocal analysis can be used to gain further insight into the nature of limited angle problems, such as laminar tomography.

Appendix A

Reconstruction Methods Used in The SVD Analysis

Here we define the two methods used to create reconstructions from simulated measurements in `analysisSVD.m`.

A.1 Truncated Singular Value Decomposition

The truncated singular value decoposition (TSVD) method is defined in terms of the SVD, in Definition 2.10, of the transformation matrix A for the system $A\mathbf{x} = \mathbf{b}$ by

$$\mathbf{x} = \sum_{i=1}^{k} \frac{\mathbf{u}_i^T \mathbf{b}}{\sigma_i} \mathbf{v}_i.$$

Where k is the truncation index and $\mathbf{x}$ is the reconstructed solution. In this thesis the TSVD method used is implemented in `analysisSVD.m`.

A.2 Landweber Method

The Landweber method is a subclass of the *simultaneous iterative reconstruction techniques* (SIRT), where each iteration is defined for the system $A\mathbf{x} = \mathbf{b}$ by

$$\mathbf{x}^{[k+1]} = \mathbf{x}^{[k]} + \lambda_k T A^T M(\mathbf{b} - A\mathbf{x}^{[k]}).$$

Where k is the iteration number and T, M are symmetric positive definite matrices. The relaxation parameter λ_k describes the step size for each iteration.

The Landweber method is then the simple case for which $T = M = \mathbf{I}$, where $\mathbf{I}$ is the identity matrix.

This thesis uses the Landweber method implemented in AIR Tools [10].

Appendix B

List of Matlab Functions

In the following is a list of the Matlab functions created for the thesis. The thesis also uses functions from the package AIR Tools [10].

All the functions listed below can be found here [9].

`main.m` - The main script used to run the analysis of Chapters 3 and 4.

`analysisSVD(data,varargin)` - Runs the analysis described in Analysis Method 3.1. Consult documentation in the function for an explanation of the input arguments.

`x = myphantom_rect(N,M)` - Creates an $N \times M$ Shepp-Logan phantom x.

`x = LaminarPhantom(N,M)` - Creates a laminar phantom x of size $N \times M$ as used in Chapter 4.

`A = changeDomain_circle(A,N)` - Changes the square $N \times N$ domain of a transformation matrix A to a circular one.

`A = changeDomain_Unitcircle(A,N)` - Changes the square $N \times N$ domain of a transformation matrix A to a unit circular one.

`A = createARadon(N,theta,p)` - Creates the transformation matrix A of `radon.m` on a $N \times N$ domain for a set of angles `theta` with p projections per angle.

The following functions are required to use some of the functionality of `analysisSVD`. The functions are not created by the authors of this thesis, but nevertheless can they be found here [9].

`suptitle.m` - Used to define a header for a group of subplots.

`distinguishable_colors.m` - Used to define distinguishable colours for each function in a plot.

`legendmarkeradjust.m` - Used to adjust the legend markers sizes.

`x = myphantom(N)` - Creates an $N \times N$ Shepp-Logan phantom x.

`x = binaryphantom(N)` - Creates a binary phantom x of size $N \times N$.

Bibliography

[1] M. J.T Littleton and M. M.L. Durizch Littleton, R.T., "Conventional tomography."

[2] P. C. Hansen, *Discrete Inverse Problems: Insight and Algorithms.* SIAM, 2010.

[3] M. Bertero et al., *Introduction to Inverse Problems in Imaging.* IOP, 1998.

[4] J. Hadamard, "Sur les problèmes aux dérivées partielles et leur signification physique," pp. 49–52, 1902.

[5] O. Christensen, *Functions, Spaces, and Expansions.* BIRKHAUSER, 2010.

[6] J. Radon, "Über die bestimmung von funktionen durch ihre integralwerte längs gewisser mannigfaltigkeiten, berichte über die verhandlungen der königlich-sächsischen," 1917.

[7] J. Frikel, *Reconstructions in limited angle x-ray tomography: Characterization of classical reconstructions and adapted curvelet sparse regularization.* Technische Universität München, Fakultät für Mathematik, 2013.

[8] P. C. Hansen, "Computation of the singular value expansion," 1987.

[9] "Matlab files for the thesis, `https://www.dropbox.com/sh/2q3drehfo68rquj/AADD1AhSn7Wi-oxC6dFy4C24a?dl=0`."

[10] P. C. Hansen and M. Saxild-Hansen, "Air tools, version 1.0."

[11] E. Akhmedov et. al., "Geotomography with sola r and supernova neutrinos," 2005.

[12] B. Povh et. al., *Particles and Nuclei: An Introduction to the Physical Concepts.* Springer, 2008.